Lawrence Berkeley National Laboratory

Title
Pore-scale capillary pressure analysis using multi-scale X-ray micromotography

Permalink
https://escholarship.org/uc/item/6944n94f

Authors
Garing, Charlotte
de Chalendar, Jacques A
Voltolini, Marco
et al.

Publication Date

DOI

Pore-scale capillary pressure analysis using multi-scale X-ray micromotography

Charlotte Garing[a,*], Jacques A. de Chalendar[a], Marco Voltolini[b], Jonathan B. Ajo-Franklin [b], Sally M. Benson [a]

[a] *Stanford University, Energy Resources Engineering, Green Earth Sciences Bldg. Rm 50, 367 Panama Street, Stanford, CA 94305, United States*
[b] *Lawrence Berkeley National Laboratory, Earth and Environmental Sciences, 1 Cyclotron Road, MS74R316C, Berkeley, CA 94720, United States*

a b s t r a c t

A multi-scale synchrotron-based X-ray microtomographic dataset of residually trapped air after gravity- driven brine imbibition was acquired for three samples with differing pore topologies and morphologies; image volumes were reconstructed with voxel sizes from 4.44 μm down to 0.64 μm. Capillary pressure distributions among the population of trapped ganglia were investigated by calculating interfacial cur- vature in order to assess the potential for remobilization of residually-trapped non-wetting ganglia due to differences in capillary pressure presented by neighbor ganglia. For each sample, sintered glass beads, Boise sandstone and Fontainebleau sandstone, sub-volumes with different voxel sizes were analyzed to quantify air/brine interfaces and interfacial curvatures and investigate the effect of image resolution on both fluid phase identification and curvature estimates. Results show that the method developed for in- terfacial curvature estimation leads to reliable capillary pressure estimates for gas ganglia. Higher resolu- tion images increase confidence in curvature calculations, especially for the sandstone samples that dis- play smaller gas-brine interfaces which are then represented by a higher number of voxels when imaged with a micron or sub-micron voxels size. The analysis of sub-volumes from the Boise and Fontainebleau dataset highlights the presence of a residually-trapped gas phase consisting of ganglia located in one or few pores and presenting significantly different capillary pressures, especially in the case of Fontainebleau sandstone. As a result, Ostwald ripening could occur, leading to gas transfer from ganglia with higher cap- illary pressure to surrounding ganglia with lower capillary pressures. More generally, at the pore-scale, most gas ganglia do present similar capillary pressures and Ostwald ripening would then not represent a major mechanism for residually-trapped gas transfer and remobilization.

1. Introduction

A critical aspect of geological carbon sequestration is the es- timation of CO_2 plume mobility and extent after injection has ceased. This estimation is particularly important in the context of open storage systems or systems in close proximity to pos- sible migration pathways e.g. permeable faults. After an initial drainage phase during injection, models typically posit that sub- stantial $scCO_2$ volumes are trapped as the plume moves under buoyant forces during brine imbibition (Kumar et al., 2005; Juanes et al., 2006; Hesse et al., 2008; Celia and Nordbotten, 2009). Con- ventional multi-phase flow models assume that residually trapped portions of the plume do not remobilize and remain stationary un- til they dissolve into the brine phase (Goodman et al., 2011), as

_____

* Corresponding author.
E-mail addresses: cgaring@stanford.edu (C. Garing), jdechalendar@stanford.edu (J.A. de Chalendar), mvoltolini@lbl.gov (M. Voltolini), JBAjo-Franklin@lbl.gov (J.B. Ajo-Franklin), smbenson@stanford.edu (S.M. Benson).

under reservoir flow conditions, viscous forces are usually not suf- ficient for mobilization. However, multiple physiochemical mecha- nisms exist which could potentially invalidate this assumption in- cluding $scCO_2$-induced transitions in wetting behavior (Kim et al., 2012; Wan et al., 2014; Wang et al., 2016), dissolution-induced ganglia size reduction (DePaolo and Cole, 2013), and inter-ganglia gas transfer via Ostwald ripening (Epstein and Plesset, 1950). In ad- dition, recent findings from fast synchrotron-based X-ray computed microtomography (Armstrong et al., 2014; Rücker et al., 2015, Arm- strong et al., 2016) and micromodel studies (Armstrong and berg, 2013) show that non- local cooperative displacement processes dur- ing water flooding have a large impact on pore scale fluid distribu- tions and ganglion dynamics and could potentially affect the sta- bility of a trapped non-wetting phase.

In this study, we seek to develop experimental methods for im- proving the understanding of one of these mechanisms, the po- tential for Ostwald ripening of the residually trapped CO_2 phase in porous media. Ostwald Ripening of gas bubbles in aqueous so- lutions has been extensively studied in homogeneous bulk media

where dispersed particles of a second phase exist in a saturated solution, and where the bigger bubbles tend to grow at the ex- pense of the smaller ones (Epstein and Plesset, 1950; Greenwood, 1956; Lifshitz and Slyozov, 1961; Voorhees, 1985; Schmelzer and Schweitzer, 1987; Möller et al., 1998). In porous media, the pres- ence of walls changes the process significantly, mainly because capillary pressure, the driver for ripening, is no longer only a func- tion of the particle radius but also of pore topology and size. Few attempts have been made to extend the study of Ostwald ripen- ing process to porous media. Most often, the process is either ne- glected (Andrew et al., 2014a), studied in a context where other mechanisms like a constant pressure decline in the liquid play a disproportionate role (Li and Yortsos, 1991; 1995; Dominguez et al., 2000), or studied in a context where cluster growth stops or is strongly inhibited once there is significant interaction with the porous matrix walls, for viscous polymers and crystals growing in a solid matrix for instance (Schmelzer et al., 1995; Möller et al., 1998). Goldobin and Brilliantov (2011) investigated the diffusion of gas in porous media using mean thermodynamic properties, but did not account for pore-scale effects.

Ostwald ripening will be driven by differences in capillary pres-
sure between gas ganglia, and subsequent diffusion of dissolved gas through the aqueous phase. Capillary pressure, which denotes the difference in pressure between a non-wetting and a wetting fluid (respectively CO_2 and brine in the case of interest), is ex- pressed by the Young-Laplace equation $P_c = P_{nw} - P_w = 2\sigma K$, where σ is the interfacial tension and K is the mean curvature of the in- terface between the two fluids. In a bulk liquid medium, a bub- ble of gas is typically spherical and its curvature is therefore di- rectly linked to the bubble size. Porous media, however, exhibit a variety of complex geometries for which no simple analytical solu- tion exists to describe the interface between two immiscible fluids. As capillary pressures inside individual non-wetting phase ganglia strongly depend on pore geometry and topology (Bear, 1972), pore- scale investigations are required in order to understand and mea- sure the distribution of capillary pressure in disconnected trapped ganglia of non-wetting phase, which is a critical question to assess Ostwald ripening mechanism.

Due to significant improvements over the last decades and its non-destructive characteristic, X-ray microtomography has become the foremost imaging technique for the visualization and quan- tification of pore-scale structures and processes as well as pro- viding input to pore-scale modeling (Blunt et al., 2013; Cnudde and Boone, 2013; Wildenschild and Sheppard, 2013, Schlüter et al., 2014). Previous authors investigated residual trapping at the pore- scale using X-ray microtomography (Prodanovic et al., 2007; Kumar et al., 2010; Iglauer et al., 2011; Tanino and Blunt, 2012; Georgiadis et al., 2013; Chaudhary et al., 2013; Andrew et al., 2014a; Rücker et al., 2015; Herring et al., 2016, Schlüter et al., 2016). In particular, all of these studies show that the residually-trapped non-wetting phase takes the form of ganglia with various sizes and complicated irregular shapes, highlighting the complexity of the non-wetting and wetting phase interface geometry, as well as of the angle both fluids form with the solid surface.
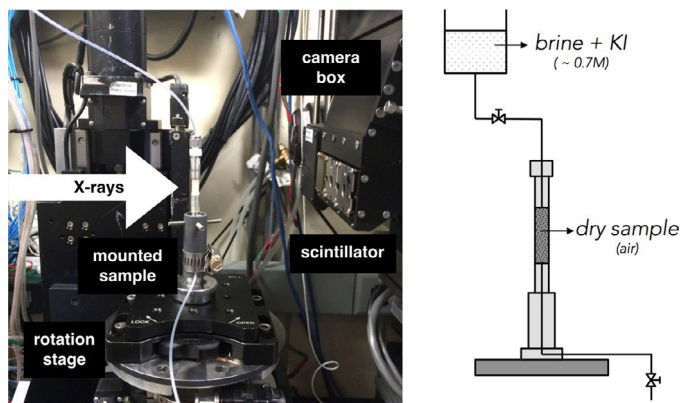
Armstrong et al. (2012a) proposed a first method to calculate
interfacial curvature using synchrotron-based X-ray microtomogra- phy images of water and oil in a glass beads packed column with a voxel size of 13 μm. They compared macro-scale capillary pressures measured via pressure transducer to micro-scale capillary pres- sures measured via interfacial curvatures calculated on the images using Avizo Software. They concluded, in particular, that higher im- age resolution was required as significant curvature errors were resulting from inadequate segmentation of small features. Follow- ing this work, Armstrong et al. (2012b) evaluated the limitations and advantages of measuring interfacial curvatures from X-ray mi- crotomography data by comparing two approaches applied to idea

spheres: the first approach measures curvature on triangular sur- faces generated at interfacial regions, as described in Armstrong et al. (2012a), the second approach measures curvature directly from an image intensity gradient. The results showed that there is an optimal amount of smoothing with either approach and, in gen- eral, the surface-based approach gave the best results. Andrew et al. (2014b) then applied the method described by Armstrong et al., (2012a) to calculate interfacial curvature of water and supercriti- cal CO_2 (scCO_2) (50 °C and 10 MPa) in a Ketton limestone sam- ple using lab-based microtomography images with a pixel size of
3.5 μm. The authors reported that curvature distributions for a sin- gle ganglion present a single well-defined peak, representing a sin- gle capillary pressure across the entire CO_2-brine interface. They also related capillary pressure measurements to local pore space topography and showed that capillary pressure was inversely pro- portional to the radius of the largest restriction surrounding the ganglion. In a recent publication aiming at identifying individual dynamic drainage events at the pore-scale using fast synchrotron- based microtomography images of scCO_2/brine in the same Ketton limestone with a voxel size of 3.64 μm, Andrew et al. (2015) ex- tended the pore-scale curvature measurement technique in order to be able to measure the smaller curvatures resulting from higher drainage capillary pressures. In particular they presented a method to select terminal menisci from the entire CO_2 ganglia interfaces using curvature anisotropy and compute the interfacial curvature using only these selected regions.

The Ostwald ripening process is driven by differences in capil- lary pressure, and consequently interfacial curvature, between gan- glia. The study of the potential for Ostwald Ripening therefore re- quires accurate methods for measuring the interfacial curvature of an individual ganglia and its associated uncertainty in a va- riety of relevant rock types. The aim of the present study is to develop reliable methods for estimating the pore-scale capillary pressure of individual residually-trapped gas ganglia for different rock types, especially sandstones, and using higher resolution im- ages in comparison to the previous studies by Armstrong et al. (2102a, 2012b) and Andrew et al. (2014b, 2015). Measurements are made on air ganglia trapped during gravitationally induced imbibi- tion. Particular attention is given to the effect of image resolution on the precision of interfacial curvature calculations. A multi-scale synchrotron-based X-ray microtomography dataset of residually- trapped gas was therefore acquired in sintered glass beads and two sandstone samples (Boise and Fontainebleau) with voxel sizes varying from 0.64 to 4.44 μm. A method to estimate the interfacial curvature was developed based on this dataset and is presented, together with a sensitivity analysis of the method to parameters such as the degree of smoothing or the number of neighbor voxels used for the calculation. For each acquired image the non-wetting (air) and wetting (brine) phases were identified, as well as the in- terfaces they share both with each other and also with the solid surface, and the connectivity and size of the trapped gas were quantified. The curvature method was then applied to the differ- ent sub-volumes chosen for analysis. The distribution of curvature values, the mean value, and associated uncertainty is presented for each disconnected air ganglion. Sub-volumes of the rock are then analyzed to determine the distribution of capillary pressures among the trapped ganglia; in particular, whether there is a statis- tically significant difference in the capillary pressures of the gan- glia trapped in the sub-volume. A detailed analysis of the impact of image resolution and interface identification on curvature esti- mates is also reported.

The key point to assess the potential for Ostwald ripening in the
investigated pore structures is to determine if neighbor gas ganglia have significantly different capillary pressures or not. Therefore a part of this work also consists in investigating the accuracy of the

2.2. Experimental set-up and protocol
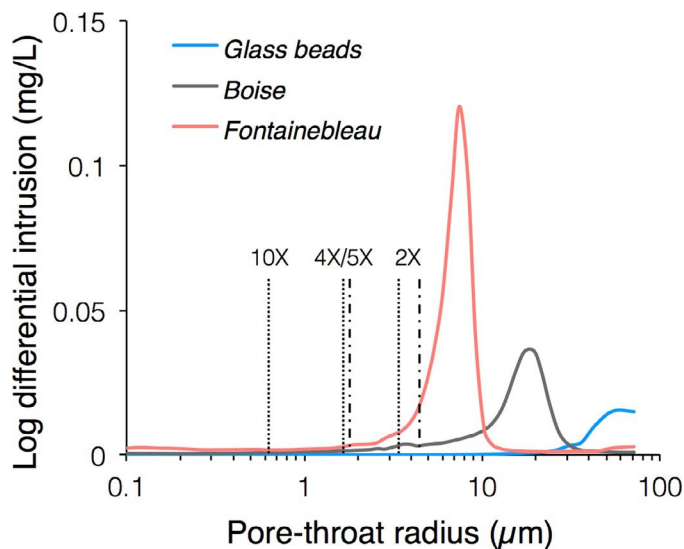
Fig. 1. Pore-throat size distribution obtained by MICP for the Glass beads (blue line), Boise sandstone (grey line) and Fontainebleau sandstone (pink line) samples presented as the differential intrusion. The voxel sizes for the different image acqui- sitions (2X – 3.28 μm for the Glass beads and Fontainebleau samples, and 4.44 μm for Boise sample / 4X – 1.62 μm for the Glass beads and Fontainebleau samples and 5X – 1.8 μm for Boise sample / 10X – 0.62 μm) are displayed with dotted and dashed vertical lines. (For interpretation of the references to color in this figure legend, the reader is referred to the web version of this article.)

method proposed in the following to calculate capillary pressure using microtomographic images.

2. Materials and methods

2.1. Rock samples

The experiments were conducted on cylindrical cores of about 6 mm diameter from three different types of samples: sintered glass-beads, Boise sandstone and Fontainebleau sandstone. The sandstones samples were cored from larger blocks while the glass bead sample was sintered in a graphite mold. The samples were selected for their significant differences in porosity and pore net- work morphology, as can be seen in Fig. 1. All of the samples are assumed to be strongly water-wet. The glass beads sample is com- posed of soda lime beads of diameters ranging from 250 to 400 μm and presents the highest porosity and pore size. Although the fo- cus of our study is on estimating capillary pressure distribution in sandstones, the glass beads sample was chosen to develop the cur- vature calculation method as large interfaces between the two flu- ids are expected. The Boise and Fontainebleau samples are quarry sandstones from Boise, Idaho (USA) and the Paris Basin (France) respectively. Fontainebleau sandstone is composed of well-sorted quartz grains only (Bourbie and Zinszner, 1985) whereas Boise sandstone contains a significant fraction of feldspar, mica, and clay materials (Zimmerman, 1984). Helium pycnometry porosity mea- surements, ϕ_{He}, were conducted on samples extracted from the same blocks in which the samples used in the experiments were cored. The respective values of porosity measured for the glass- beads, Boise and Fontainebleau samples are 0.40, 0.28 and 0.10. Mercury injection capillary pressure analysis (MICP) was also per- formed and the pore-throat diameter distributions are shown in Fig. 1. The corresponding mean diameters d_{Hg} are 101 μm, 31 μm and 14 μm for the Glass beads, Boise and Fontainebleau samples, respectively.

Gravity-driven imbibition of water into an air-filled rock sam- ple was used to create a residually trapped air phase. The samples were wrapped in a heat-shrink PTFE tube and mounted vertically on the rotating stage in the beamline hutch, as displayed in Fig. 2. The inlet and outlet, both wrapped together with the sample to as- sure fluid flow through the core, were connected to flexible tubing allowing rotation during scanning. Two valves were placed at the inlet and the outlet side in order to isolate the sample. The inlet tubing was also connected to a small reservoir located at an up- per height so that gravity-driven imbibition could be performed: a solution of deionized water and 0.7 mol/L potassium iodide, serv- ing as a contrast agent, was poured in the reservoir and could then flow at room pressure and temperature through the dry sample by gravity leaving behind a fraction of trapped air. Both valves were closed after brine came out of the outlet valve and the system was left immobile 30 min to reach equilibrium before scanning.

2.3. Data acquisition

The dataset was acquired at the beamline (BL) 8.3.2. of the Advanced Light Source (Lawrence Berkeley National Laboratory). Cross-sections through each imaged volume are displayed in Fig. 3. In each case, a baseline scan of the dry sample was first acquired, then multiple scans at different resolutions were taken after the imbibition process. The entire dataset was acquired using two dif- ferent optics configuration, leading to slightly different resulting voxel sizes for the Glass beads and Fontainebleau sandstone sam- ples and for the Boise sandstone sample, as detailed below. The raw data are available on The Digital Rocks Portal (Garing et al., 2017, Prodanovic et al., 2015)

2.3.1. Glass beads and Fontainebleau sandstone

For both samples, a set of 2049 projections was acquired using a PCO.Edge camera with an Optique Peter system; 2X (3.28 μm), 4X (1.62 μm) and 10X (0.64 μm) objectives were used as well as a multilayer monochromator set to 25 keV. The following exposure times were selected: 450 ms, 1200 ms and 1500 ms for the Glass beads 2X, 4X and 10X scans respectively; 475 ms and 1500 ms for the Fontainebleau 2X and 4X-10X scans respectively.

2.3.2. Boise sandstone

A set of 1441 projections was acquired using a PCO.4000 cam- era with normal optics 2X (4.44 μm voxel size) and 5X (1.80 μm voxel size) at an energy of 32 keV. Exposure times of 800 ms and 1000 ms were selected for the 2X and 5X scans respectively.
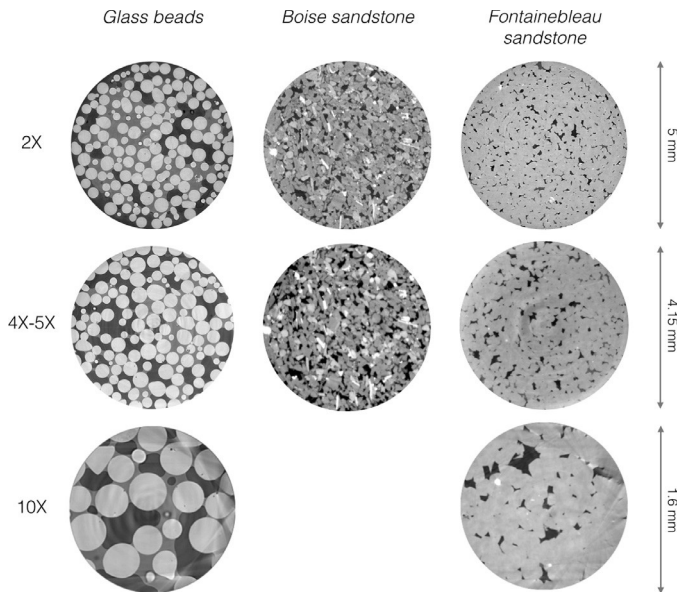
Fig. 3. Two-dimensional cross sections through the 3D reconstructed volumes for the Glass beads, Boise sandstone and Fontainebleau sandstone imaged with different magnification resulting in multiple resolutions: 2X-4X-10X, respective voxel sizes of 3.28 μm-1.62 μm-0.64 μm, for the glass beads and Fontainebleau sandstone samples and 2X-5X, respective voxel sizes of 4.44 μm-1.8 μm, for the Boise sandstone sample.

The reconstruction of the volumes was performed using two different procedures, depending on the contrast needed in the datasets: i) a standard filtered back-projection, using a Shepp– Logan filter (Kak and Slaney, 1987) applied to the flat-field cor- rected projections, ii) a single-distance phase retrieval algorithm on the projections which improves the contrast among the dif- ferent phases and reduces phase contrast artifacts. The algo- rithm presented by Paganin et al. (2002) and implemented in the ANKAphase software package (Weitkamp et al., 2011) was chosen for phase retrieval. The reconstruction was then performed using a conventional filtered back-projection algorithm with the Octopus software (Dierick et al., 2004).

The voxels are coded in terms of grey levels depending on the
X-ray beam attenuation. The solid matrix appears in light grey, the brine in medium grey and the air in dark grey (Fig. 3).

2.4. Image analysis

Once the 3D volume is reconstructed, a sequence of post- processing steps is required in order to quantify the fluid phase distribution, connectivity, cluster size, pore diameter or interfacial curvature. The successive steps are detailed below and illustrated in Fig. 4 on a cropped volume of Boise sandstone BS-5X (voxel size of 1.80 μm). The image processing was conducted using Fiji, Avizo Fire 9 and MATLAB programs.

2.4.1. Segmentation, connectivity and size

All segmentations were performed on the raw reconstructed scans directly due to the good quality of the imaging process, ex- cept for BS-2X data (Boise sandstone, voxel size of 4.44 μm) for which an edge-preserving noise reduction filter such as bilateral filter (Tomasi and Maduchi, 1998) was first applied first in or- der to reduce the noise. The segmentation of the three different phases, solid, brine, and gas, was carried out via visual inspection of the datasets and gray level histogram using Fiji package. The brine segment was cleaned via a conventional procedure including median filtering and/or binary morphological operators, combined

with masking (i.e. a Boolean AND operator) with the original seg- mented dataset. This procedure allows recovering the finer details of the objects erased by the structuring element shape and size used in the noise-reducing procedures. This approach is especially useful when dealing with binary datasets, where any filtering can significantly affect the morphology of the objects, and in our spe- cific case it allowed more precise borders, as if segmented directly from the original unfiltered dataset, and especially correct solid- gas interfaces. Examples of 2D raw and segmented images are pre- sented for the glass beads (Fig. 4.1 and 2), the Fontainebleau sand- stone (Fig. 4.3 and 4) and the Boise sandstone (Fig. 4.a and b) sam- ples. The entire image processing workflow is displayed for the lat- ter sub-volume (Fig. 4.a–h). Each smaller sub-volume investigated was re-segmented using the same method than for the larger vol- umes for more accurate results. The number of voxels belonging to the pore phase V_p and belonging to the air phase V_{air} are com- puted and since the entire number of voxels composing the ana- lyzed rock volume V_{tot} is also known, the total porosity $\phi_{\mu CT}$ and air saturation S_{nw} can be calculated as V_p/V_{tot} and V_{air}/V_p respec- tively. The connectivity of both fluid phases, air and brine, is then quantified by analyzing the data in 3D (Fig 4.c and d.). Each dis- connected cluster is identified and re-labeled and its volume is computed. In addition, the equivalent diameter distribution of the air phase, brine phase and pore space (air and brine grouped as a unique phase) was computed by generating distance maps and recording the diameter of maximum inscribed spheres. Both con- nectivity and equivalent diameter analysis were conducted using Avizo Fire 9 Software.

#### 2.4.3. Interfacial curvature

This subsection describes the workflow for the method devel- oped to compute interfacial curvature of gas clusters using the seg- mented micro-CT images, where voxels belong to one of the three identified phases (rock, brine or gas). The main steps consist of finding and meshing the surface of the gas phase; restricting it to the interface shared with the brine phase; smoothing the result- ing mesh; and calculating the corresponding curvature, as detailed below. All steps are performed by a in-house MATLAB code specif- ically developed for this study.

2.4.3.1. Meshing the interface. The surfaces of the gas and brine phases are identified by using the MATLAB (MathWorks) function *isosurface,* an implementation of the Marching Cubes algorithm, leading to a trigonal mesh representing the surface of the gas phase

together with a list of vertices that belongs to both gas and brine surfaces, which describe the interface under consideration (Fig. 4.e). In order to deal with potential edge effects at the line of contact where there is a discontinuity in curvature, the in-house code developed by the authors deletes the vertices that belong to the rock/gas interfaces from the mesh before applying smoothing and computing the curvature. This in contrast with previous stud- ies where a commercial software is used and the user must wait for the end result to heuristically prune unrealistic curvature val- ues (Andrew et al., 2015).

2.4.3.2. *Smoothing the surface.* The mesh resulting from the pre- vious steps is smoothed using an implicit fairing method of the type described in Desbrun et al. (1999). This smoothing method attenuates noise in the mesh through a diffusion process: a lin- ear approximation of the mesh Laplacian is computed and used (via implicit integration in time of a heat diffusion type equation) to disperse small disturbances and smooth high frequencies while keeping the main shape intact. Specifically, we consider a mesh X with m vertices x_i, $i = 1 \bullet \bullet \bullet m$ and integrate the following equation over time:

$$\frac{\partial X}{\partial t} = \lambda L(X)$$
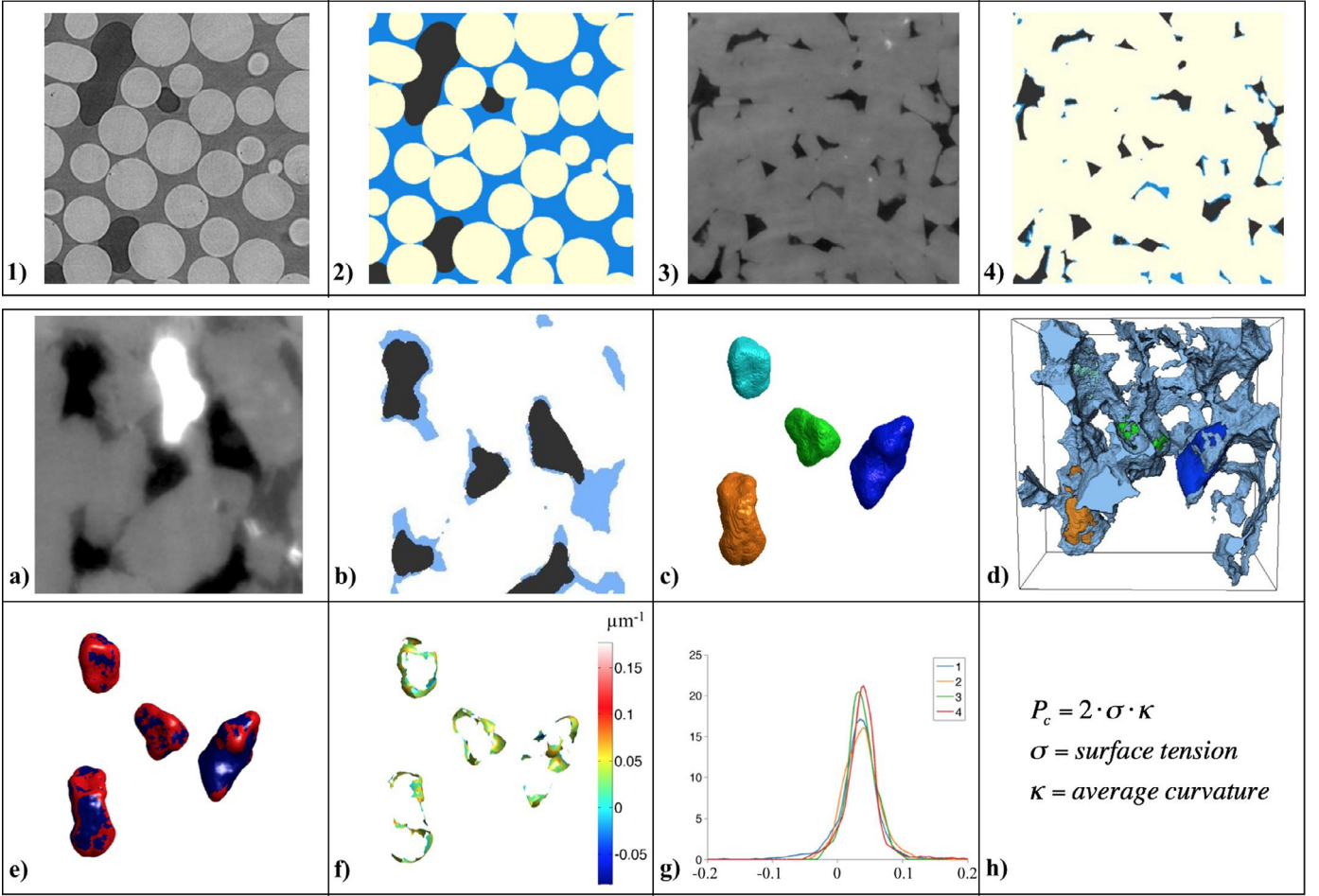
Fig. 4. Examples of 2D raw image after reconstruction and the corresponding 2D segmented image of the glass beads sample (1) and (2) respectively) and the Fontainebleau sandstone sample (3) and (4) respectively); Three phases are identified: the solid matrix (yellow), the air (black) and the brine (blue). The entire image processing workflow is then presented for a cropped sub-volume of Boise sandstone 5X (290*290*140 voxels with a voxel size of 1.80 μm). **a)** 2D raw image. **b)** 2D segmented image. **c)** 3D rendering of the separated air clusters, or ganglia. **d)** 3D rendering of the air ganglia together with the brine phase (light blue). **e)** Visualization of the interfaces with the brine phase presented by each gas ganglion. **f)** The mean curvature is calculated for each point of the air/brine interface. **g)** The curvature histograms are extracted and a mean curvature value can be calculated for each gas ganglion and for the entire investigated volume. **h)** The capillary pressure is calculated using the computed mean curvature and the appropriate surface tension value. (For interpretation of the references to color in this figure legend, the reader is referred to the web version of this article.)

where $L(X)$ is the mesh Laplacian and λ is a parameter (taken to be 1 in our application).

More details on Laplacian mesh processing can be found in Sorkine (2006). An explicit Euler scheme is used to integrate Eq. (1):

$$Xn+1 = (I + \lambda \delta tL)X n \qquad (2)$$

We call T_{max} the time for which the mesh is smoothed. It means that Eq. (2) will be used $[T_{max}/\delta t]$ times. Fig. 5 shows an example of the impact of smoothing, T_{max} ranging from 0 (raw mesh) to 6 (18 iterations of the heat diffusion procedure with a time step δt of 0.3), for a single air ganglia isolated from (**a**) the glass beads sam- ple imaged with a voxel size of 0.64 μm and (**b**) the Boise sand- stone sample imaged with a voxel size of 1.8 μm. The curvature estimates rapidly converge once a small amount of smoothing is applied, as previously reported by Andrew et al. (2014a). We chose a value of $T_{max} = 5$ and $\delta t = 0.3$ for the following.

2.4.3.3. Estimating the curvature of a mesh. For any point P on a surface, we can define the unit normal vector $n(P)$. The deriva- tive of n at P defines the shape operator whose eigenvectors and eigenvalues are the principal directions and principal curvatures (Federer, 1959). If $K_1(P)$ and $K_2(P)$ denote the principal curvatures

at point P, the mean curvature is $K(P)=(K_1(P)+ K_2(P))/2$ and the Gaussian curvature is $\Gamma(P)=K_1(P) \cdot K_2(P)$. In this paper the term curvature is generically used to denote the mean curvature $K(P)$ at point P. A classic approach to compute the curvature of a mesh is to locally approximate it using quadric surfaces, whose curva- ture can be calculated analytically. Another approach described in Cohen-Steiner and Morvan (2003) consists of redefining curvature in the context of normal cycle theory so that the definition now holds for polygonal surfaces. This work builds on the observation that the curvature measures of a smooth surface can be obtained from an object associated to the surface called the normal cycle of the surface and that the definition of the normal cycle of a surface has a unique natural extension to the case of a polyhedral surface (a mesh). G. Peyre implemented an algorithm in MATLAB as well as other useful graph theory utilities that are used in this work for curvature calculations (Peyre, 2007). In the end, a mean curvature estimate is obtained for each vertex of the air/brine interface (Fig. 4.f).

The method involves a parameter corresponding to the number of neighbors, $N_{neighbors}$, over which the curvature tensor is averaged when it is calculated at each vertex. Fig. 5 shows the impact of av- eraging related to the number of neighbors chosen, $N_{neighbors}$ rang-
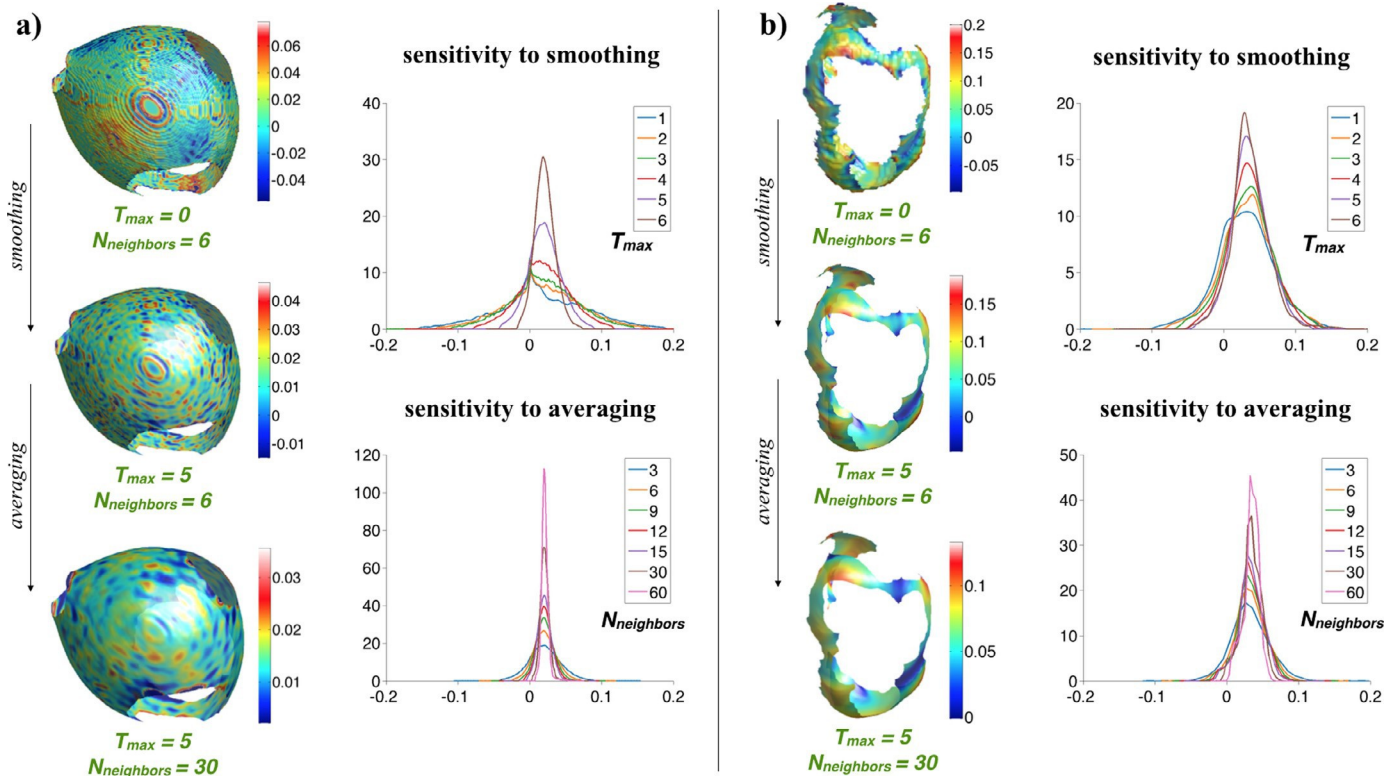
Fig. 5. Sensitivity analysis performed on a single air ganglia isolated from **a)** the glass beads sample imaged with a voxel size of 0.64 μm and **b)** and from the Boise sample images with a voxel size of 1.8 μm: effect of smoothing (T_{max}) and averaging ($N_{neighbors}$) on the mean curvature calculated using the normal cycle method.

ing from 3 to 60, for the single air ganglia isolated from (**a**) the glass beads sample imaged with a voxel size of 0.64 μm and (**b**) the Boise sandstone sample imaged with a voxel size of 1.8 μm. For both cases, the graphs suggest that the curvature estimates are similar when selecting a higher number of neighbors for the cal- culations, the distribution functions becoming however less spread out when averaging on more neighbors, as expected. In order to stay relatively close to the real data we chose to $N_{neighbors} = 7$ in the following.

For several isolated ganglia we also performed curvature calcu- lations using an implementation of the quadric fitting algorithm in MATLAB (Kroon, 2011) and using the corresponding implemen- tation in the Avizo Fire package (FEI). The three calculations lead to similar mean curvature values, especially once some smoothing was applied to the mesh. We decided to use our own developed code for more flexibility and we chose to use the normal cycle al- gorithm due to the fact that the quadric fitting method may be prone to instability, as the algorithm requires inverting matrices that can be ill-conditioned.

2.4.3.4. Estimating capillary pressures. The curvature estimates ob- tained for the entire air/brine interface can be investigated for each disconnected gas ganglion. Curvature distributions for each ganglion are plotted as probability distribution functions (Fig. 4.g) and an average mean curvature K is calculated for each ganglion.

high resolution of the images and nature of the pore-space, brine films are detected between the ganglia and rock surface. In these regions, the ganglia are supported by the rock, not the interfacial tension between the gas and the liquid and therefore these flat in- terfaces should be removed for curvature calculations. Identifying the vertices that belong to the thin films is however not trivial. We first handled this issue by deleting the connected components of the mesh that have negative curvature values and represent a large number of voxels.

2.4.3.6. Statistics. Confidence intervals were calculated using the classic expression for the Standard Error of the mean $SE = SD/\sqrt{n}$, where SD is the sample standard deviation and n is the number of samples. Assuming normal distributions, the true mean of the dis- tribution we are sampling from has a 95% probability to be within $1.96 \cdot SE$ away from the mean. When applied to a single ganglion, these confidence intervals give a measure of how well the capillary pressure of an individual disconnected ganglion can be estimated. For a single ganglion the following nomenclature is used: the mean curvature, which is the average of all curvature values calculated for each points of the interface, is noted K and the standard devia- tion and error for the ganglion are respectively noted SD_g and SE_g. Average values for the entire population of ganglia are indicated by The corresponding average mean capillary pressure P_c is then esti- mated assuming that Laplace's law, $P_c = 2 \cdot \sigma \cdot K$ (Fig. 4.h), is valid Average values for the entire population of ganglia are indicated by $\_\cdot\_$, where , where X (X)/N ganglia. The average ganglion stan-

for the unsupported interface of the gas ganglia and using an in- terfacial tension σ for air and water of 72 mN.m^{-1} (Vargaftik et al., 1983).

2.4.3.5. Fontainebleau sandstone. A slightly different procedure was applied to the Fontainebleau sandstone dataset where, due to the

The corresponding average mean capillary pressure P_c is then esti-mated assuming that Laplace's law, $P_c = 2 \cdot \sigma \cdot K$ (Fig. 4. h), is valid for the unsupported interface of the gas ganglia and using an in-terfacial tension σ for air and water of 72 mN.m -1 (Vargaftik et al., 1983).

dard deviation and error for the population of ganglia are therefore noted SD_g and respectively, and k and P_c refer to the average mean curvature and capillary pressure for a given sample. Finally the standard deviations of the ganglia mean curvature and ganglia capillary pressure for the entire ganglia population of a sample are noted SD_K and SD_{Pc} respectively.

Table 1

Characteristics of the sub-samples investigated using multi-scale X-ray microtomography: name of the sub-sample, voxel size (length of the side of the cube forming the voxel [μm]), volume [mm³], computed porosity $\phi_{\mu CT}$ and air saturation S_{nw}, number of separated air ganglia *Ntot ganglia* and number of these ganglia presenting an interface with the brine phase large enough for the interfacial curvature analysis *N ganglia*.

Rock Sample	μCT Images	Voxel size (μm)	V (mm³)	$\phi_{\mu CT}$ (-)	Snw (-)	Ntot ganglia	N ganglia
Glass beads	GB-2X*	3.28	8.3	0.36	0.19	5	5
	GB-4X*	1.62	1	0.37	0.81	3	3
Boise	BS-2X⁺	4.44	1.3	0.19	0.60	90	73
	BS-5X⁺	1.80	1.3	0.18	0.66	122	90
	BS-5X*	1.80	1	0.25	0.40	114	102
	BS-5X°	1.80	0.48	0.29	0.53	49	38
Fontainebleau	FS-4X*	1.62	1	0.07	0.72	157	107
	FS-10X*	0.64	0.05	0.06	0.75	26	20

3. Results

The first part of this section presents the results for the anal-ysis of fluid phase distribution and morphology for the three in-vestigated rock samples, with a presentation of the air and brine distribution, connectivity and equivalent diameter, and air ganglia size. This first subsection aims at characterizing the three differ-ent pore structures and their corresponding fluid phase distribu-tion and morphology in relation with the image resolution in or-der to determine the appropriate resolution and volume required for each rock type for an accurate identification of representative air/brine interfaces.

The second part of this section first presents curvature calcula-tions results for single ganglia, with a focus on the impact of image resolution and interface identification on how well the capillary pressure in one ganglion can be estimated. The curvature and cap-illary pressure calculations for the population of ganglia presented by all the sub-samples analyzed are then presented for each rock type.

3.1. Fluid phase distribution and morphology

For each dataset available the results are presented for all the sub-samples on which the detailed analysis were performed (Table 1). Porosity $\phi_{\mu CT}$ and air saturation S_{nw} were also computed on larger volumes to assess the representative character of the sub-volumes. The results are available in supplementary material Table S1.

3.1.1. Air and brine distribution and connectivity

For each rock type the fluid phase distribution was investigated by analyzing a same sub-volumes of 1 mm³ imaged with compa-rable voxel size (1.62 μm for the Glass beads and Fontainebleau sub-samples, respectively GB-4X* and FS-4X*; and 1.80 μm for the Boise sub-sample BS-5X*). The results are displayed in Fig. 6. For each rock type, the results were compared with sub-samples im-aged with lower and/or higher resolution.
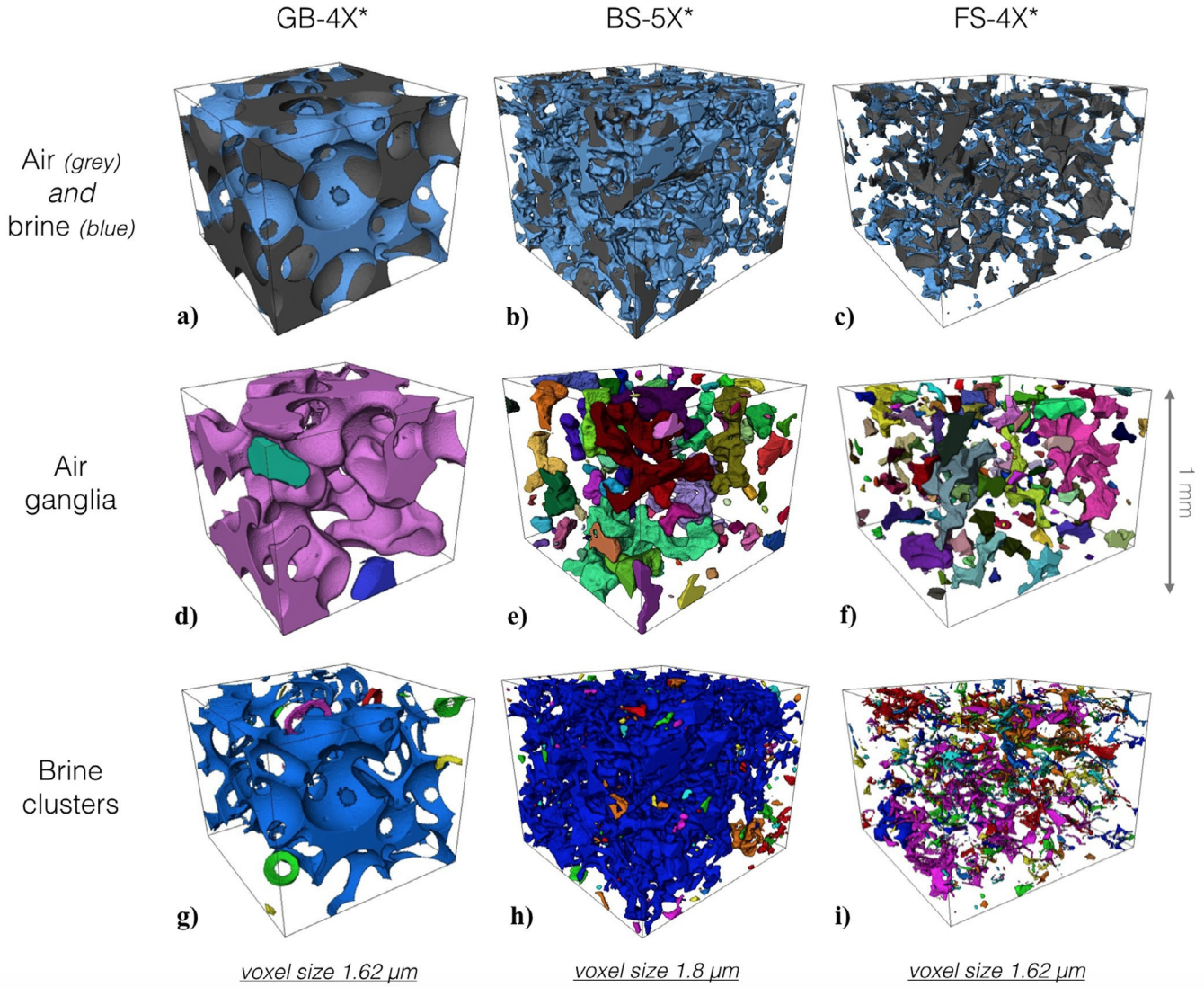
The glass beads sub-sample has the highest porosity (0.37) and air saturation (0.81) and presents the largest interfaces between the two fluid phases (Fig. 6.a). The residual air phase forms a large connected cluster representing 98% of the air phase (Fig. 6.b), and the brine phase is also well connected with some locally discon-nected brine identified as pendular rings between beads (Fig. 6.c), as previously reported by Armstrong et al. (2012a). The analysis of a larger sub-volume of the glass beads sample imaged with a lower resolution shows that the sub-sample displays a similar porosity (Table 1) and a much lower air saturation, which however corre-sponds to the value computed on the large volume with the same resolution (Table S1). The characteristics of the fluid phases are

very similar between the two sub-samples, with one large well-connected cluster spanning through the whole volume (Fig. 8.a) and large interfaces with a well-connected brine phase (Fig. 9.b). Considering the fluid configuration, the image acquired with the highest resolution (GB-10X) implying a much smaller volume sam-pled, was not analyzed for curvature calculation purpose.

The sandstone samples have very different pore space size dis-tributions and topologies in comparison to the glass beads sam-ple, and have distinct fluid phase distributions and morphologies. Looking first at the 1 mm³-cubes, the results show that although the two sub-samples exhibit different values of porosity (0.25 for Boise and 0.07 for Fontainebleau) and air saturation (0.40 for Boise and 0.72 for Fontainebleau), they both present a residual air phase that consists of a large number of disconnected air ganglia with a high fraction of small size ganglia and few larger ones, as displayed in Fig. 6.e and Fig. 6.f for Boise and Fontainebleau respectively. In the case of the Boise sub-sample, the air phase presents a no-ticeably large fraction of interfaces with the brine phase (Fig. 6.b) and the brine phase forms a large well-connected cluster span-ning throughout the sub-volume, with few small-size disconnected clusters (Fig. 6.h). Fig. 6.c shows that there are fewer interfaces between the air and brine phases for the Fontainebleau 1 mm³-cube and that they consist of much smaller features. One should note the high air saturation for this sample. With a voxel size of 1.62 μm, the brine phase appears as very poorly connected, as it consists of a high number of small size disconnected clusters of brine (Fig. 6.i).

The analysis of a larger and a smaller sub-volume the Boise sample imaged with the same voxels size of 1.80 μm (BS-5X⁺ and BS-5X° respectively) that there is a noticeable discrepancy between computed porosity and air saturation for each sub-volume, with porosity values ranging from 0.18 to 0.25 and air saturation val-ues ranging from 0.40 to 0.66 (Table 1). However, the three sub-samples present very similar fluid phase distribution, with a high number of disconnected air ganglia (Fig. 10.e, i and m) and well-identified interfaces with the brine phase (Fig. 10.f, j and n). A comparison with the lower resolution was also conducted by an-alyzing the exact same sub-volume of 1.3 mm³ imaged with a voxel size of 1.8 μm (BS-5X⁺) and a voxel size of 4.44 μm (BS-2X⁺). The computed porosity values are very close and the air satura-tion computed on BS-2X⁺ is lower than for BS-5X⁺, as listed in Table 1. In general the large to medium size air clusters are identi-cally identified for both sub-samples but smaller air ganglia are not identified for BS-2X⁺ (Fig. 10.a and e). The most difference comes from the identification of the air/brine interfaces. Although they appear localized at the same parts of the air ganglia, the interfaces are much smaller for BS-2X⁺ (Fig. 10.b and f).

Finally, a smaller sub-volume of the Fontainebleau sample im-aged with the highest resolution was also analyzed (FS-10X*). The

	GB-4X*	BS-5X*	FS-4X*

Air (grey) and brine (blue)

Air ganglia

1 mm

Brine clusters

voxel size 1.62 µm   voxel size 1.8 µm   voxel size 1.62 µm

Fig. 6. 3D rendering of fluid phase distribution and connectivity in 1 mm³ sub-volumes of the three rock samples imaged with similar resolution and named GB-4X*, BS-5X* and FS-4X* for the Glass beads, Boise sandstone and Fontainebleau sandstone sample, respectively. **a), b)** and **c)**: air (dark grey) and brine (blue) phase distribution in the pore space. **d), e)** and **f)**: disconnected air ganglia represented with different colors. **g), h)** and **i)** clusters formed by the brine phase. As for the air ganglia different clusters are displayed with different colors. (For interpretation of the references to color in this figure legend, the reader is referred to the web version of this article.)

porosity and air saturation computed on this sub-sample are similar to the ones computed on the 1 mm³-cube imaged with the intermediate resolution (Table 1). As for the Boise samples, the fluid phase distribution is very similar between the two sub-samples with an air phase consisting in many disconnected angular-shaped air ganglia (Fig. 11.**a** and **e**) presenting thin interfaces with the brine phase (Fig. 11.**b** and **f**). One can note that a high portion of the air/brine interfaces consist in thin films between the air ganglia and the solid matrix. Due to the small features presented by the brine phase and the interfaces with the trapped gas, the image acquired with the lower resolution (FS-2X) was not used for curvature calculations.

3.1.2. Air and brine equivalent diameter

The mean equivalent diameter presented by the air and brine phase, as well as by the entire pore-structure saturated with air and brine, were analyzed for the 1 mm³-cubes presented in the previous sub-section. The mean values are listed in Table 2 and the distributions are displayed in Fig. 7.
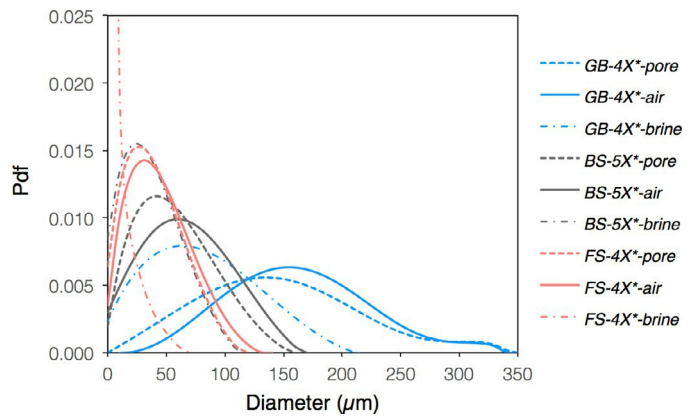
Fig. 7. Equivalent diameter distribution of the pores (dashed lines), air (solid lines) and brine (dashed-dotted lines) phase expressed as fitted probability density func- tion pdf for the Glass beads sub-sample GB-4X* (blue lines), Boise sandstone sub- sample BS-5X* (grey lines) and Fontainebleau sub-sample FS-4X* (pink lines) of 1 mm³. (For interpretation of the references to color in this figure legend, the reader is referred to the web version of this article.)

Table 2

Mean equivalent diameter of the pore, air and brine phase computed on the 1 mm³ sub-volumes of the glass beads (GB-4X*), Boise (BS- 5X*) and Fontainebleau (FS-4X*) samples. The mean pore throat di- ameter d_{Hg} estimated using MICP is reminded in the last column.

μCT images	Voxel size (μm)	Mean equivalent diameter (μm)			d_{Hg} (μm)
		pore	air	brine	
GB-4X*	1.62	147	148	87	101
BS-5X*	1.80	62	68	43	31
FS-4X*	1.62	39	52	11	14
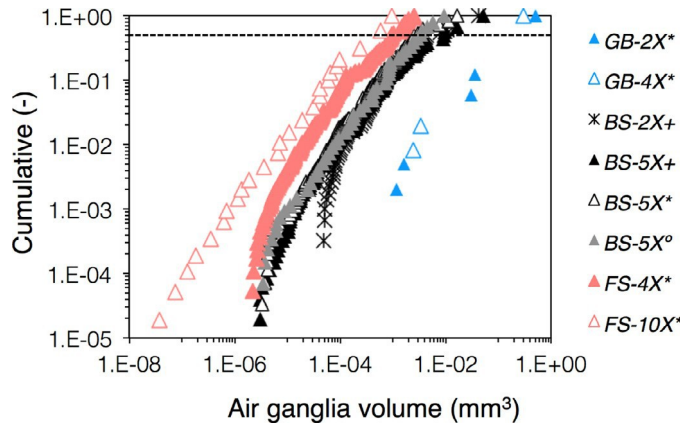
Fig. 8. Cumulative air ganglia volume. The dotted line indicates half of the air phase volume (cumulative of 0.5). The results are presented for the different sub- samples investigated for the Boise sample imaged with a voxel size of 4.44 μm (BS- 2X+) and 1.8 μm (BS-5X+, BS-5X* and BS-5X°) – black and grey symbols, and for the Fontainebleau sample imaged with a voxel size of 1.62 μm (FS-4X*) and 0.64 μm (FS-10X*) – pink symbols. (For interpretation of the references to color in this figure legend, the reader is referred to the web version of this article.)

The results shows that both the air and brine phase of the Glass beads sample presents large geometries and that the mean equivalent diameter of the air phase is similar as the one of the pore space. For the Boise sample, the mean equivalent diameter of the phase presenting the smallest features, the brine phase, is slightly higher than the mean pore-throat diameter estimated with MICP (31 μm) and corresponds to about 20 voxels. In contrary, the mean diameter of the brine phase for the Fontainebleau sample is smaller than the mean pore-throat diameter (14 μm) and the dis- tribution plot confirms that a significant fraction of the brine phase is of a size smaller than the image resolution of the 4X dataset.

3.1.3. Residual air ganglia size

For all the sandstone sub-samples, the air ganglia size (volume) and their distribution were analyzed. The results are displayed in Fig. 8 and additional details are provided in supplementary Table S2. The 1 mm³-cube from the Boise sample (BS-5X*) contains 114 air ganglia (Table 1) with a mean volume of 1.8E-4 mm³, equiv- alent to the volume of a sphere of about 70 μm diameter. The largest ganglion represents 17.2% of the total air phase and the seven largest ganglia accounts for 50% of the air phase. As ex- pected, for a same resolution, the number of identified discon- nected clusters depends on the volume of the sub-sample analyzed (Table 1). However, the mean air ganglia volume is almost identical for the three sub-volumes BS-5X+, BS-5X* and BS-5X° (Table S2) as is the air ganglia volume distribution (Fig. 8). When comparing an identical volume imaged with two different resolution (BS-2X+ and BS-5X+), the results shows that although fewer disconnected air ganglia are identified with the lower resolution, the mean air ganglia volume is in the same order of magnitude (Table S2) and the air ganglia volume distribution is almost identical (Fig. 8).

The 1 mm³-cube from the Fontainebleau sample (FS-4X*) has a larger number of air ganglia than the Boise sub-sample of same volume (Table 1): the air phase consists of 157 disconnected gan- glia. The mean volume of these ganglia is 6.6E-5 mm³, which would be equivalent to a sphere of 50 μm diameter, and is 2.7 times smaller than for BS-5X*. The largest ganglion represents a smaller fraction of the total air phase (12.9%) and also more gan- glia are required to account for 50% of the air phase (Table S2, Fig. 8). When comparing with the highest resolution, less and one or- der of magnitude smaller size air ganglia are identified for FS-10X* than for FS-4X* but it should be noted that in that case the total volume analyzed is also much smaller for FS-10X* (0.05 mm³) than for FS-4X* (1 mm³).

3.2. Interfacial curvature

#### 3.2.1. Calculation of the capillary pressure in an individual ganglion

Before investigating the capillary pressure of all the ganglia identified for each sub-volume presented in the previous section, a first analysis of the impact of image resolution and interface iden- tification on curvature calculations, hence capillary pressure esti- mates, was conducted on single isolated ganglia.

The effect of image resolution on the calculation of interfacial curvature was investigated by analyzing the same air ganglion that could be identified on two images of the same sample acquired with different image resolutions. The analysis was conducted on an isolated air ganglion for the glass beads sample imaged with a voxel size of 1.62 μm and 0.64 μm, GB-4X and GB-10X respec- tively (Fig. 9.a), the Boise sample imaged with a voxel size of 4.44 μm and 1.80 μm, BS-2X and BS-5X respectively (Fig. 9.b) and the Fontainebleau sample imaged with a voxel size of 1.62 μm and 0.64 μm, FS-4X and FS-10X respectively (Fig. 9.c). Details regard- ing the curvature calculations are given in Table 3.a. For the glass beads sample the isolated air bubble present similar characteris- tics with both resolutions: the shape and volume of the bubble

is almost identical as is the interface with the brine phase and its curvature. The mean value K is 0.0219 μm^{-1} for GB-4X and 0.0226 μm^{-1} for GB-10X, leading to similar mean capillary pressure P_c of 3148 Pa and 3260 Pa for GB-4X and GB-10X respectively. The standard errors are low and lead to 95% confidence intervals of $\pm$ 24 Pa and $\pm$ 12 Pa for the GB-4X and GB-10X bubble respectively.

The results differ in the case of the sandstone samples. For both the Boise and Fontainebleau samples, the air ganglia identi- fied present some discrepancy although the general shape is pre- served and total volume is in the same order of magnitude. For all cases one can note that the volume is lower with higher resolu- tion. Fig 9.b and c also shows that the portion of the air surfaces that is shared with the brine phase is roughly located on the same parts of the air ganglia. However, due to a very different num- ber of points representing the identified interfaces with the differ- ent image resolution (lower with bigger voxel sizes), the interface that remains after the image processing for the curvature calcula- tion highly differs. For the Boise sample, the final mean value K is 0.0309 μm^{-1} for BS-2X and 0.0483 μm^{-1} for BS-5X, leading to capillary pressure P_c of 4450 Pa and 6955 Pa for BS-2X and BS-5X ganglia respectively. The standards errors are higher than for the Glass beads ganglion. The corresponding 95% confidence intervals in terms of capillary pressure are $\pm$ 240 Pa and $\pm$ 201 Pa for BS- 2X and BS-5X respectively. For the Fontainebleau sample, there are not enough voxels left after processing to estimate the curvature of the FS-4X ganglion. The mean curvature calculated on the FS-10X ganglion is 0.124 μm^{-1}, which corresponds to a capillary pressure of 17,903 Pa. For this ganglion the 95% confidence interval on the capillary calculation is $\pm$ 453 Pa.

The local variation of the curvature estimation on the interface was also investigated in order to assess the impact of interface
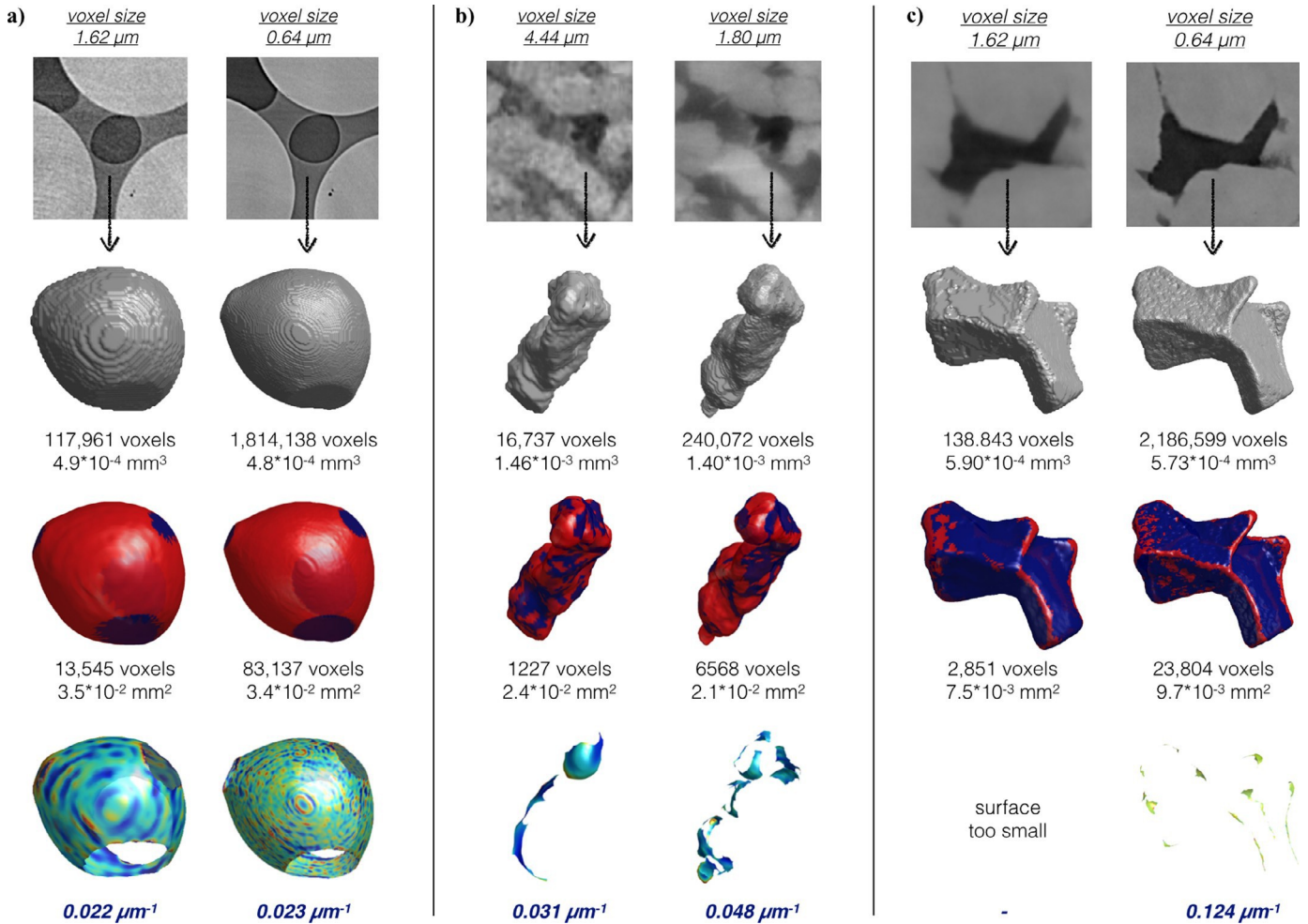
Fig. 9. Effect of image resolution on curvature estimation analyzed for the same air ganglion isolated from **a)** the glass bead sample imaged with a voxels size of 1.62 μm (GB-4X) and 0.64 μm (GB-10X), **b)** the Boise sample imaged with a voxel size of 4.44 μm (BS-2X) and 1.8 μm (BS-5X) and **c)** the Fontainebleau sample imaged with a voxel size of 1.62 μm (FS-4X) and 0.64 μm (FS-10X). In each case, the Figure shows from top to bottom for both resolution: a 2D raw image, the 3D segmented air ganglion (with its volume in voxels and mm^3), the visualization of the interface in red (with its surface in pixels and mm^2), and the visualization of the mean curvature values presented by the interface. The details are provided in Table 3.a. (For interpretation of the references to color in this figure legend, the reader is referred to the web version of this article.)

identification on the curvature calculation, as the air/brine inter- face presented by a single air ganglion may change depending on the image acquisition, resolution and image processing. This analy- sis was conducted on the well-defined air ganglia isolated from the glass beads sample imaged with a voxel size of 0.64 μm (GB-10X) and from the Boise sample imaged with a voxel size of 1.8 μm (BS- 5X) that have been used for the sensitivity analysis presented in Section 2.4.3. For each isolated air ganglion, regions were selected randomly on the interface and the curvature was computed for the selected portions of the total interface, as displayed in Fig. 10, and detailed in Table 3.b. The calculation using the entire interface is the first raw, marked in bold. The results show that the seven se- lected portions of interface of the isolated ganglia extracted from GB-10X dataset present similar interfacial curvature distributions (Fig. 10.a) and curvature values K, ranging from 0.016 μm^{-1} to

0.023 μm^{-1}, with an average of 0.021 μm^{-1} and a standard devi- ation from one K calculation to another of 0.002 μm^{-1}. On aver-

age, the values calculated on the selected interfaces differ from the one calculated using the entire identified interface by a bit less than 10%. There is more discrepancy in curvature distributions between the different interfaces selected from the BS-5X ganglion (Fig. 10.b). The curvature values for the different portions of the interface range from 0.027 μm^{-1} to 0.043 μm^{-1}, with an average

of 0.034 μm^{-1} and a standard deviation of 0.007 μm^{-1} and differ from the one calculated using the entire interface by 17%. In gen- eral one can also note that the standard error of the mean cur- vature and capillary pressure is lower when the entire identified interface is used for calculation since it involves a higher number of points where the mean curvature is computed when averaging for the ganglion.

3.2.2. Curvature analysis for the different rock types

This sub-section presents the results of interfacial curvature cal- culations and capillary pressures the different sub-volumes ana- lyzed for each rock type. The results of the curvature analysis are displayed in Fig. 11–13 for the sub-volumes of the Glass beads, Boise and Fontainebleau sample respectively. Each figure displays the results similarly: the results for a sub-volume are organized in column, where the first image is a visualization of the discon- nected air ganglia, the second is a visualization of the air/brine interfaces, the third image is a visualization of the all the mean curvature values displayed by the interfaces taken into account for the mean calculation, and the last image is a graph of the pdfs for the curvature values for each air ganglion. The average curva- ture of each ganglion is then plotted as a function of its total vol- ume in Fig. 14. The results are also presented in terms of capillary
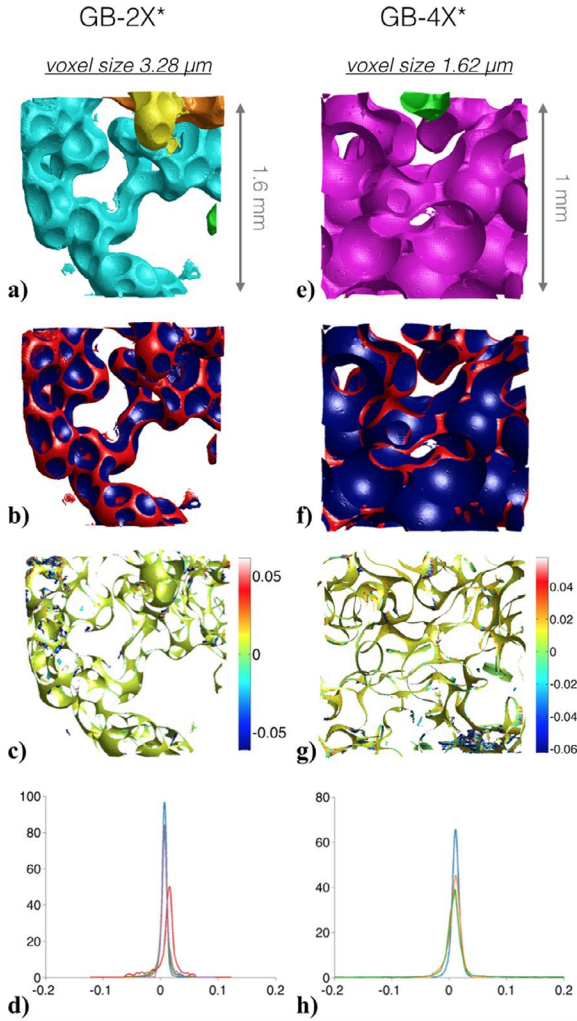
Table 3

(a) Effect of image resolution: interfacial curvature analysis conducted on the same air ganglion isolated from images acquired with different voxel sizes for the glass bead (GB-4X, GB-10X), Boise (BS-2X, BS-5X) and Fontainebleau (FS-4X, FS-10X) samples, displayed in Fig. 9. b) Location on the mesh: interfacial curvature analysis conducted on selected portions of the entire interface of air ganglia isolated from the glass bead (GB-10X) and Boise (BS-5X) samples, displayed in Fig. 10. The calculation performed on the entire interface is highlighted in bold. For both a) and b) the Table lists the voxel size, the number of points on the interface used for the calculation, mean curvature K for the ganglion, standard deviation SDg and standard error SEg of curvature values calculated for each point of the interface, mean ganglion capillary pressure Pc, and standard error of capillary pressure values for the ganglion.

	µCT images	Voxel size (µm)	N points interface	K (μm^{-1})	SDg (μm^{-1})	SEg (μm^{-1})	Pc (Pa)	SE_{Pc} (Pa)
a)	**GB-4X**	1.62	13,545	0.0219	0.0099	8.51E-05	3148	12
	GB-10X	0.64	83,137	0.0226	0.0126	4.36E-05	3260	6
	BS-2X	4.44	1227	0.0309	0.0298	8.52E-04	4450	123
	BS-5X	2.8	6568	0.0483	0.0577	7.12E-04	6955	103
	FS-4X	1.62	0	–	–	–	–	–
	FS-10X	0.64	6328	0.1243	0.1276	1.60E-03	17,903	231
b)		0.64	**83,137**	**0.0226**	**0.0126**	**4.36E-05**	**3260**	**6**
			2025	0.0222	0.0207	4.59E-04	3191	66
	GB-10X		1631	0.0220	0.0219	5.42E-04	3174	78
	isolated		2041	0.0213	0.0222	4.92E-04	3060	71
	ganglia		1604	0.0232	0.0240	6.00E-04	3347	86
			3975	0.0200	0.0214	3.40E-04	2875	49
			3343	0.0201	0.0226	3.90E-04	2887	56
			1347	0.0157	0.0203	5.54E-04	2254	80
		1.80	**4628**	**0.0371**	**0.0216**	**3.17E-04**	**5347**	**46**
	BS-5X		293	0.0431	0.0207	1.21E-03	6210	174
	isolated		262	0.0271	0.0189	1.17E-03	3908	168
	ganglia		466	0.0388	0.0219	1.01E-03	5594	146
			988	0.0301	0.0271	8.61E-04	4336	124
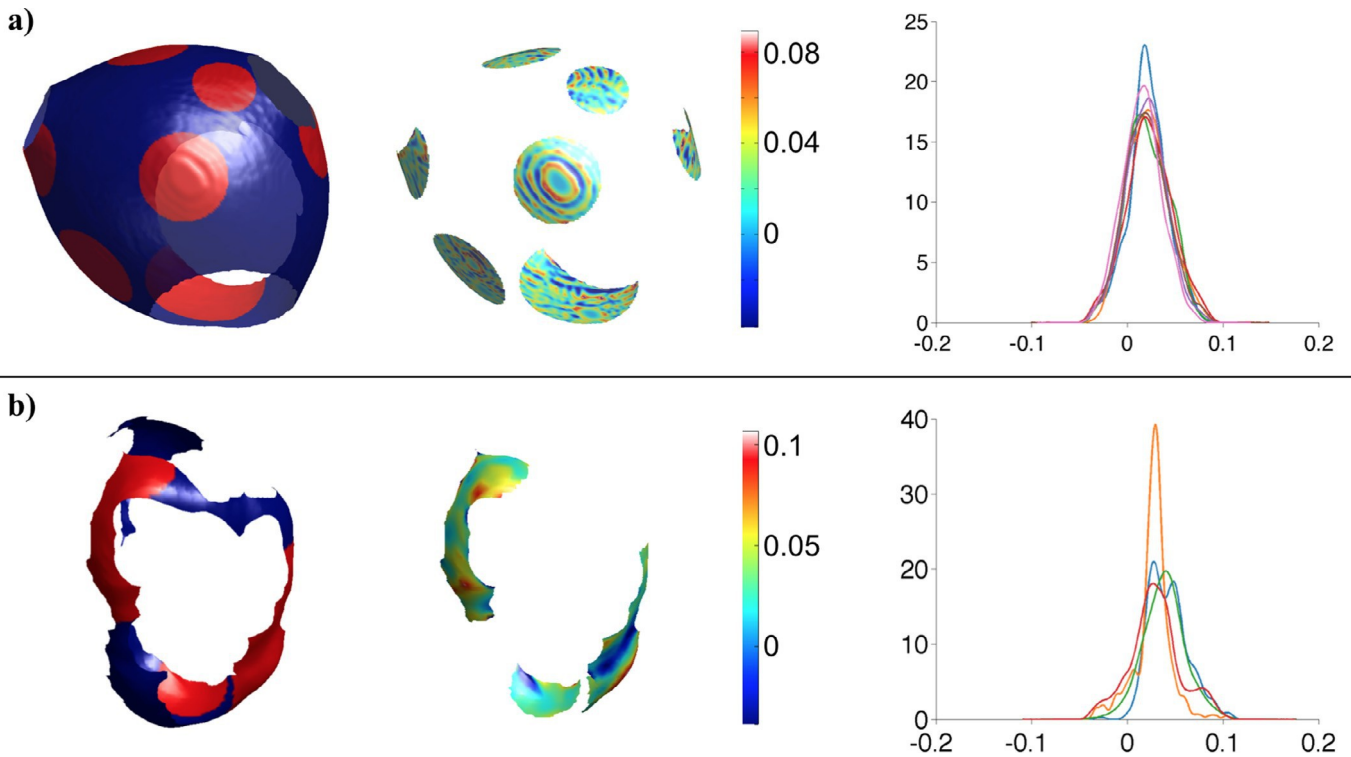
Fig. 10. Local variation of the curvature estimation on the interface analyzed for a single air ganglia isolated from **a)** the glass beads sample imaged with a voxel size of 0.64 µm (GB-10X) and **b)** the Boise sample imaged with a voxel size of 1.8 µm (BS-5X). In each case, the Figure shows from left to right: a visualization of the selected portions of the interface (red), a visualization of the mean curvature values presented by the selected interfaces, and a plot of the corresponding curvature histograms. The details are provided in Table 3.b. (For interpretation of the references to color in this figure legend, the reader is referred to the web version of this article.)

GB-2X*
voxel size 3.28 μm

GB-4X*
voxel size 1.62 μm

a) 1.6 mm

e) 1 mm

b) f)

c) (scale: 0.05, 0, -0.05)

g) (scale: 0.04, 0.02, 0, -0.02, -0.04, -0.06)

d)

h)

volumes are low and corresponds to 95% confidence interval of ± 33 and ± 65 Pa, in terms of capillary pressure, for GB-2X* and GB-4X* respectively. The distributions graphs also show that the curvature values for each isolated air ganglia are similar one to another, as also clearly represented in Fig. 14.a. The average curvature k is 0.008 $μm^{-1}$ and 0.015 $μm^{-1}$ for GB-2X* and GB-4X* respectively, corresponding to mean capillary pressures P_c of 1107 Pa and 2139 Pa for GB-2X* and GB-4X* respectively. It should be reminded that the two sub-volumes do not sample the same volume within the Glass-Beads sample.

Fig. 11. Interfacial curvature analysis for the analyzed sub-volumes of the glass beads sample imaged with a voxel size of 3.28 μm (GB-2X* - graphs **a)** to **d)**) and of 1.62 μm (GB-4X* - graphs **e)** to **h)**). **a)** and **e)** the disconnected air ganglia are represented with different colors. **b)** and **f)** the total air phase is represented in navy blue and the interfaces with the brine phase are colored in red. **c)** and **g)** the mean curvature is plotted for each portion of interface used for the calculation. **d)** and **h)** the mean curvature distribution is plotted for each separated air ganglion that presents interfaces large enough for the calculation. (For interpretation of the references to color in this figure legend, the reader is referred to the web version of this article.)

pressure distributions for both sandstone samples in Fig. 15. These results are also summarized in Table 4 where the average standard deviation and standard error of the mean for the curvature values presented by the interface of a single ganglion, SD_g and SE_g respectively, are first listed, followed by the average mean curvature value presented by all the ganglia, k, and the standard deviation of the ganglia average curvature values SD_K, as well as the corresponding average capillary pressure value (P_c) and standard deviations, (P_c) and SD_{Pc} (cf last paragraph of Section 2.4.3).

3.2.3. Glass beads subsamples (GB-2X*, GB-4X*)

Fig. 11.c and g highlight the similarity of curvature values presented by the interfaces considered for the calculation. For both sub-volumes, the distributions of curvature values for each isolated air ganglia (Fig. 11.d and h) show that the interfaces of all identi- fied ganglia present similar local values of mean curvature that are close to the average mean value for the ganglia. For a single air cluster, the average standard errors of the mean for the two sub-

3.2.4. Boise subsamples (BS-2X+, BS-5X+, BS-5X*, BS-5X°)

Fig. 12. c, g, k and o display visualizations of the curvature val- ues presented by the interfaces considered for the calculation for BS-2X+, BS-5X+, BS-5X* and BS-5X° respectively. The correspond- ing curvature distribution histograms per air ganglia are shown in Fig. 12.d, h, l and p. The results are detailed for the three sub- volumes of the sample imaged with a voxel size of 1.8 μm, and then for the sub-volume of the sample imaged with a voxel size of 4.44 μm (BS-2X+), which represents the exact same volume as BS-5X+.

For the three sub-volumes imaged with a voxel size of 1.8 μm, Fig. 12.h, l and p show that the interfaces of all disconnected air ganglia present more broadly distributed local values of mean cur- vature around the average mean value for the ganglia than for the glass beads sub-volumes presented above. On average, the stan- dard error of the mean for a single ganglia SE_g is similar for all three sub-samples and is low, corresponding to 95% confidence in- tervals in terms of capillary pressure around ± 490 Pa. When com- pared with BS-5X+, the air ganglia for BS-2X+ presents a higher standard error for a single ganglion, leading to more than three times higher 95% confidence interval (± 2287 Pa).

There is a significant discrepancy in the average ganglia curva- ture values K in between the three different sub-volume images with the same resolution (Table 4) leading to mean capillary pres- sure estimates of 5782; 7803 and 4617 for BS-5X+, BS-5X* and BS- 5X° respectively. However, one can note that the average mean cur- vature for the sub-volume images with the lower resolution (BS- 2X+) is very close to the value calculated for BS-5X+. The standard deviation of the mean curvature presented by the different air gan- glia is 0.020 $μm^{-1}$ for both BS-5X+ and BS-5X° and is a bit higher for BS-5X* with a value of 0.033 $μm^{-1}$ (Table 2, Fig. 14.b). In ad- dition, the figure highlights that the air ganglia

presenting a mean curvature value that differs the most from the average are usually within the smallest ganglia, in terms of volume. It also shows that sub-volume BS-2X$^+$ presents a higher fraction of air ganglia with interfacial curvature values that are scattered further from the av- erage value for the entire sub-volume. The standard deviation for that sub-volume is 0.042 μm^{-1}. However, in that case, it is not par- ticularly correlated with the air ganglia volume.
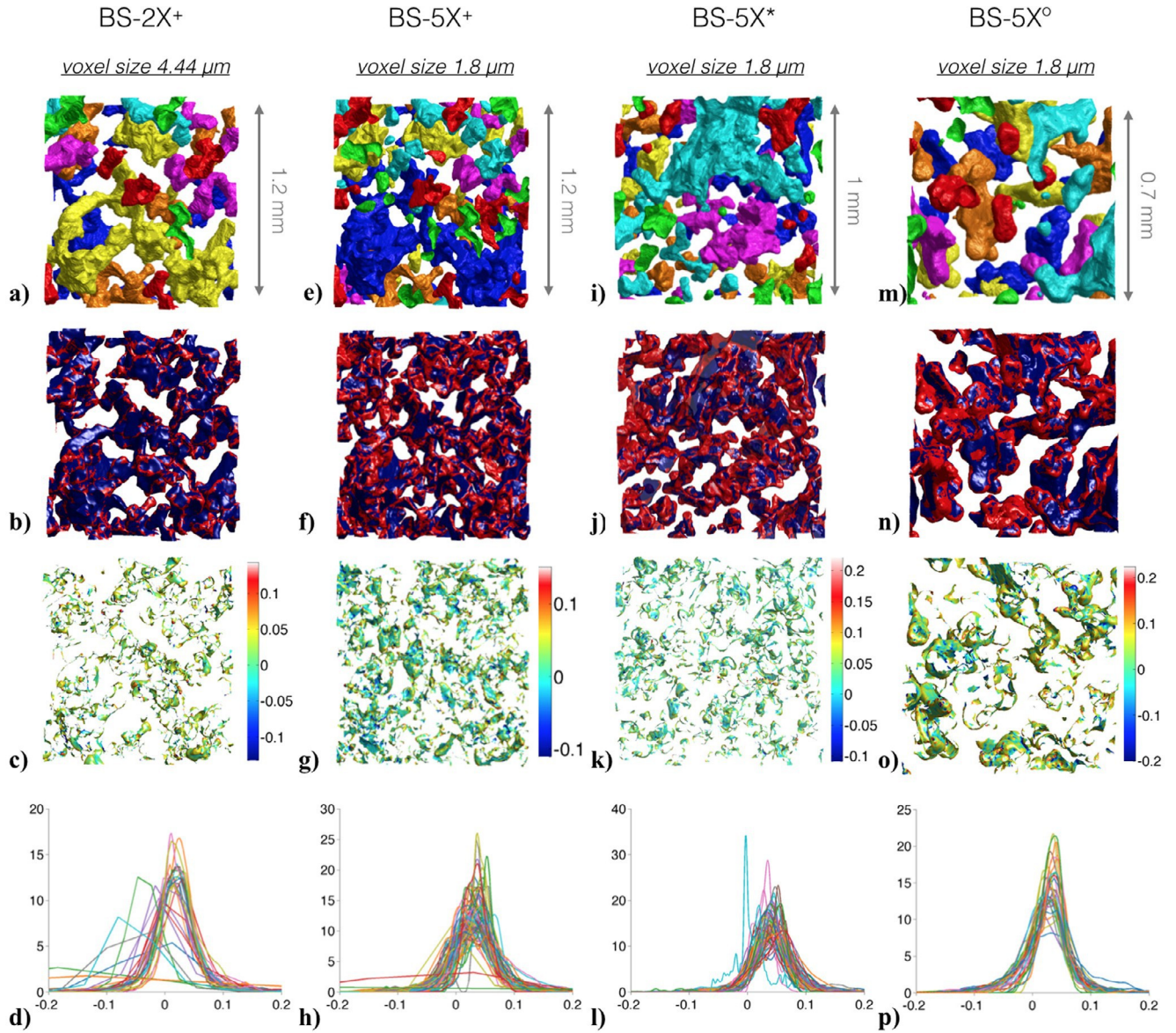
3.2.5. Fontainebleau subsamples (FS-4X*, FS-10X*)

Although Fig. 13.c and g show that both sub-samples FS-4X* and FS-10X* present rather similar interfacial curvature, the dis- tributions of curvature values for each isolated air ganglia differs (Fig. 13.d and h): whereas for FS-4X* most ganglia present simi- lar distributions, the distributions presented by the air ganglia for FS-10X* vary from a ganglion to another and the deviation is also larger. These results include however all the interfaces that re- main after deleting from the mesh the vertices that belong to the rock/air interface as explained in Section 2.4.3, which is the pro- cedure that was successfully applied to the glass beads and Boise images. As mentioned in the Material and Methods section, a high fraction of flat air/brine interfaces are still present in the case of the Fontainebleau sandstone, due to the presence of thin films be- tween the air phase and the rock. These interfaces, which are likely
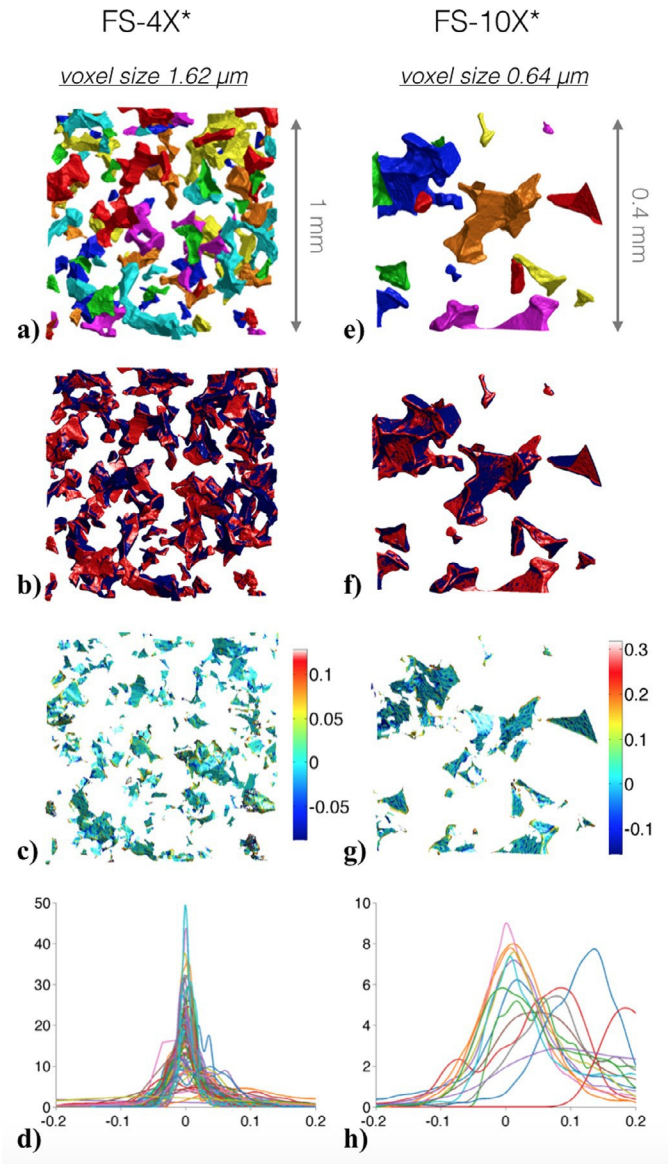
Table 4

Curvature analysis results for all the sub-volumes analyzed (more details regarding the sub-volumes can be found in Table 1. They all sample different volumes of the Glass-beads, Boise or Fontainebleau images, except BS-2X$^+$ and BS-5X$^+$ which correspond to the exact same volume of Boise sample im- aged with two different voxel sizes). For each image the table lists its name, voxel size, number of ganglia N ganglia, average standard deviation SDg a( ) ( ) curvature values for a ganglion, the average curvature presented by the ganglia (the standard deviation of the ganglia curvature values SD_K, the average capillary pressure presented by the ganglia ( ) and the standard deviation of the capillary pressure values SD_{Pc}.

µCT images	Voxel size (µm)	N ganglia	<SDg> (µm^{-1})	<SEg> (µm^{-1})	<K> (µm^{-1})	SD$_K$ (µm^{-1})	<Pc> (Pa)	SD$_{Pc}$ (Pa)
GB-2X*	3.28	5	0.009	1.2E-04	0.008	0.002	1107	308
GB-4X*	1.62	3	0.011	2.3E-04	0.015	0.008	2139	1173
BS-2X$^+$	4.44	73	0.234	8.1E-03	0.042	0.042	6071	6106
BS-5X$^+$	1.80	90	0.068	1.8E-03	0.040	0.020	5782	2957
BS-5X*	1.80	102	0.066	1.8E-03	0.054	0.033	7803	4742
BS-5X°	1.80	38	0.061	1.7E-03	0.032	0.020	4617	2889
FS-4X*	1.62	107	0.205	1.0E-02	0.110	0.113	15,893	16,340
FS-10X*	0.64	20	0.099	3.1E-03	0.147	0.093	21,110	13,401

BS-2X$^+$ — voxel size 4.44 µm (a, b, c, d); 1.2 mm

BS-5X$^+$ — voxel size 1.8 µm (e, f, g, h); 1.2 mm

BS-5X* — voxel size 1.8 µm (i, j, k, l); 1 mm

BS-5X° — voxel size 1.8 µm (m, n, o, p); 0.7 mm

Fig. 12. Interfacial curvature analysis for the analyzed sub-volumes of the Boise sandstone sample imaged with a voxel size of 4.44 µm (BS-2X$^+$ - figures **a)** to **d)**) and of 1.8 µm (BS-5X$^+$ - figures **e)** to **h)**, BS-5X* - figures **i)** to **l)** and BS-5X° - graphs **m)** to **p)**). **a), e), i)** and **m)** the disconnected air ganglia are represented with different colors. **b), f), j)** and **n)** the total air phase is represented in navy blue and the interfaces with the brine phase are colored in red. **c), g), k)** and **o)** the mean curvature is plotted for each portion of interface used for the calculation. **d), h), l)** and **p)** the mean curvature distribution is plotted for each separated air ganglion that presents interfaces large enough for the calculation. (For interpretation of the references to color in this figure legend, the reader is referred to the web version of this article.)

FS-4X*

voxel size 1.62 µm

FS-10X*

voxel size 0.64 µm

1 mm

0.4 mm

a)

e)

b)

f)

c)

0.1
0.05
0
-0.05

g)

0.3
0.2
0.1
0
-0.1

d)

50
40
30
20
10
0
-0.2   -0.1   0   0.1   0.2

h)

10
8
6
4
2
0
-0.2   -0.1   0   0.1   0.2

Fig. 13. Interfacial curvature analysis for the analyzed sub-volumes of the glass beads sample imaged with a voxel size of 1.62 µm (FS-4X* - graphs **a)** to **d)**) and of 0.64 µm (FS-10X* - graphs **e)** to **h)**). **a)** and **e)** the disconnected air ganglia are rep- resented with different colors. **b)** and **f)** the total air phase is represented in navy blue and the interfaces with the brine phase are colored in red. **c)** and **g)** the mean curvature is plotted for each portion of interface used for the calculation. **d)** and **h)** the mean curvature distribution is plotted for each separated air ganglion that presents interfaces large enough for the calculation. (For interpretation of the ref- erences to color in this figure legend, the reader is referred to the web version of this article.)

ent air ganglia is also higher for the lower resolution sub-sample (Figs. 14.c and 15). As already noticed for Boise sub-samples, Fig. 14.c also highlights that higher curvature values are more frequent for air ganglia of smaller volume.

4. Discussion

4.1. Identifying gas ganglia and gas/brine interfaces

Since the ability to accurately characterize the trapped non-wetting phase and identify the interface shared with the wetting phase is an important factor to estimate capillary pressure distri-bution in rocks using interfacial curvature calculations on X-ray microtomography images, this issue was addressed first. As ex-pected, it is highly dependent on both i) the pore size and shape of the scanned rock sample and ii) the image resolution of the scans.

to be supported by the solid, significantly lower the mean interfa- cial curvature values of air ganglia and were therefore removed for the curvature calculation listed in Table 4 and displayed in Figs. 14 and 15.

The average standard error of the mean, for a single ganglion, is on average one order of magnitude higher for FS-4X* than for FS-10X*, and also generally higher than for Boise sandstone. It cor- responds to 95% confidence intervals in terms of capillary pressure of $\pm$ 3096 Pa for the lower resolution and $\pm$ 874 Pa for the higher resolution. The average ganglia curvature values K are also differ- ent for the two sub-volumes, leading to mean capillary pressure estimates of 15,893 Pa for FS-4X* and 21,110 Pa for FS-10X*. The standard deviation of the mean curvature presented by the differ-

4.1.1. Glass beads

Porous samples which have a pore structure consisting of well- connected flow paths of large diameter and low or moderate pore body to pore throat ratio, represented here by the glass beads sam- ple, display large nonwetting and wetting phase features with very clearly identifiable interfaces between the two fluids. The glass beads sample presents a mean pore-throat diameter, estimated with MICP, about 30 times larger than the lower image resolution (GB-2X, voxel size of 3.28 µm) and even the smaller features, pre- sented by the brine phase, are more than one order of magnitude larger than the highest voxel size. Although the same object would be described by more voxels using higher resolution images, all the features are still represented by a very high number of voxels at the lower magnification. In addition, the use of the lower res- olution allows imaging of a larger volume. Even though the glass beads pore space is very homogeneous and could be well repre- sented by a smaller volume, the trapped gas consists of a single well-connected cluster spanning through most of the sample. This is in good agreement with previous X-ray microtomography anal- ysis of trapped nonwetting phase in water-wet glass beads packs conducted by Armstrong et al. (2012a), Chaudhary et al. (2013) and Georgiadis et al. (2013). For such rock types displaying a well- connected large pore structure, the volume of the sample becomes more critical for fluid flow investigations than the voxel size.

Although this is not directly in the scope of the paper, it is

worth mentioning that, for this sample, the large difference in sat- uration between the 2X and 4X scans is due to movement of fluid phases in between the two image acquisitions. Motion artifacts were actually still present on the 10X scans. This suggests that for such pore morphologies, the residual trapping process seem to re- quire longer equilibration time than usually assumed. Armstrong et al. (2012a) reported that 20 min was not enough. The present study suggests that even five hours is not sufficient to have complete equilibrium in this class of systems. Recent work from McClure et   al. (2016a, 2016b) also indicates that relaxation times for curva- tures may range from several hours to a day.

4.1.2. Sandstones

If one considers that at least three voxels are required as a min- imum to correctly identify an object, then the images acquired with the 2X magnification (voxel sizes of 4.44 µm for Boise and

3.28 µm for Glass beads and Fontainebleau) could not unambigu- ously probe any features smaller than about 10–13 µm. Fig. 1 in- dicates that 20% and 30% of the pore network exists below this threshold for the Boise and Fontainebleau samples respectively. Therefore, whereas this resolution is sufficient to accurately probe the pore network displayed by the Glass beads sample, higher res- olution is needed for a more precise characterization of the mi- crostructure for these standard sandstone samples. The compari-
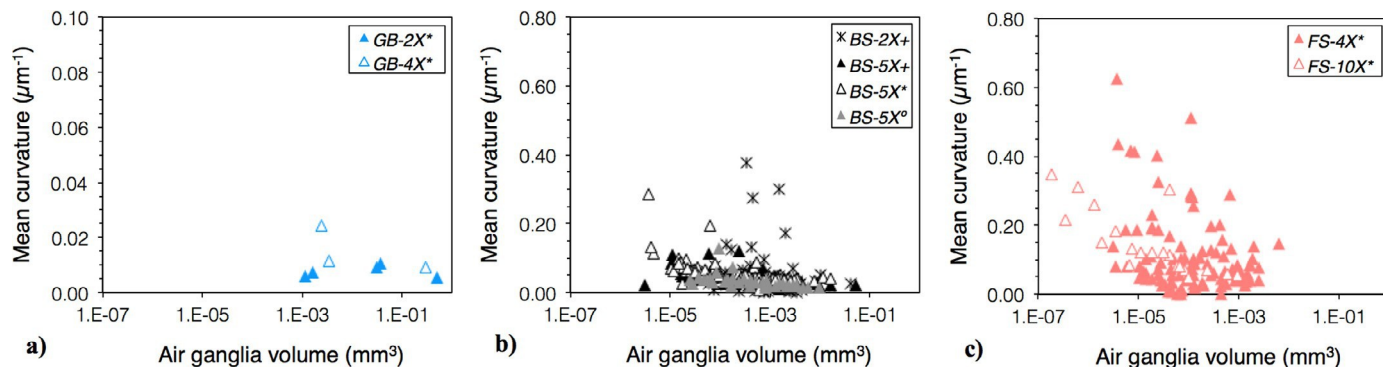
Fig. 14. Air ganglia mean curvature [μm^{-1}] as a function of the air ganglia volume [mm^3] for the analyzed sub-volumes of **a)** the glass beads sample, **b)** the Boise sandstone sample and **c)** the Fontainebleau sandstone sample.
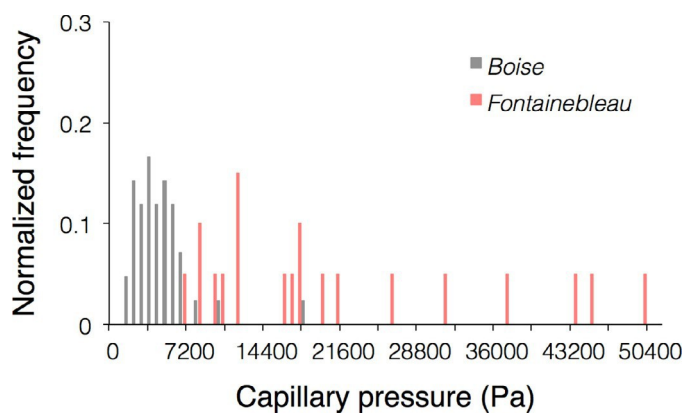

Fig. 15. Capillary pressure distribution for Boise sandstone sample (represented by sub-sample BS-5X°) and Fontainebleau sandstone sample (represented by sub-sample FS-10X*).

son of porosity and saturation values computed on different sub-volumes confirms that Boise sandstone is more heterogeneous than Fontainebleau sandstone. Boise microstructure is unique and quite different than the average sandstone due to quartz overgrowth bridges as well as the abundance of platy mica grains (Prasad, 2001). Laminations present in the sample lead to more variabil- ity and an overall significant heterogeneity of the pore structure. The data also show that Fontainebleau sandstone exhibits a higher residual gas saturation. In Fontainebleau sandstones, the reduc- tion of porosity by quartz overgrowths around the grains leads to angular pores between quartz grains of moderate size and very thin planar pores between two grains (Bourbie and Zinszner, 1985). This pore space morphology, characterized by a large as- pect ratio between the pore bodies and throats is known to fa- vor trapping by snap-off (Tanino and Blunt, 2012). Hamon et al. (2001) measured residual gas saturation in different types of sand- stones, including a similar Fontainebleau sample, and reported that Fontainebleau trapped much more gas (70% saturation) than the other shaly samples, comparable to Boise sandstone (40–50% maxi- mum saturation). Sok et al. (2002) performed imbibition site-based invasion percolation simulations on Fontainebleau sandstone net- works and also concluded in higher gas saturation for low porosity Fontainebleau.

The sub-volumes of 1 mm^3 investigated for the two sandstones with voxel sizes around 1.7 μm sample a large amount of discon- nected ganglia (114 for Boise and 157 for Fontainebleau) and the

largest ganglia contribute to less than 20% of the total gas phase (17.2% for Boise and 12.9% for Fontainebleau); we can then as- sume that these volumes are well representative of the gas gan- glia distribution. Because of the heterogeneity of Boise sandstone different sub-volumes might present different porosity and fluid saturation values; however, the characteristics of the air phase is very consistent. The cluster size analysis of air ganglia for all dif- ferent sub-volumes investigated for Boise sandstone show indeed very similar results, with air ganglia volumes distributed over four orders of magnitude. The distribution of air ganglia volume dis- plays a similar trend for Fontainebleau sandstone but with gener- ally smaller air ganglia. Iglauer et al. (2011) showed that Dodding- ton sandstone was trapping clusters from a hundred voxels to ten thousands voxels. Andrew et al. (2014a) also reported that signifi- cant proportions of scCO$_2$ is trapped in various sandstone and car- bonate samples in clusters with sizes ranging over five orders of magnitude, with better connected pore spaces having more large clusters relative to small clusters. This is supported by the compar- ison of the results for the Fontainebleau sandstone presented in this study and results reported by Kumar et al. (2010) for a more porous Fontainebleau sample, exhibiting larger pore sizes and bet- ter connectivity; in this case, the authors imaged larger size clus- ters that may span more than hundreds of pores. For both sand- stones investigated in the present paper, the mean air ganglia vol- ume estimated from the cluster size study suggests that despite the presence of few large air ganglia spanning a larger number of pore bodies and throats, most disconnected air ganglia are located in one or few pores. The most significant difference between the two sandstones lies in the size and shape of the interfaces that gas ganglia share with the brine phase. For Boise sandstone the equiv- alent diameter for the brine phase is larger than the throat diam- eter estimated with MICP and both are larger than the voxels size. However, in the case of Fontainebleau sandstone the equivalent di- ameter for the brine phase is smaller than the MICP throat diam- eter and is close to the size of few voxels. This is both due to the very high gas saturation, hence low fraction of brine in the sample, and the fact that the wetting phase occupies the smallest part of the pore space, which in the case of Fontainebleau sandstone can be very close to the voxels size. In order to

have a better identifica- tion of the interfaces for curvature calculations the highest resolu- tion (voxel size of 0.64 μm) is necessary for rocks presenting sim- ilar pore and throat sizes than those displayed by Fontainebleau sandstone, whereas the medium resolution (voxels size of 1.8 μm) allows a good representation of the interfaces for Boise sandstone   or any type of rocks presenting a similar pore space topology and morphology.
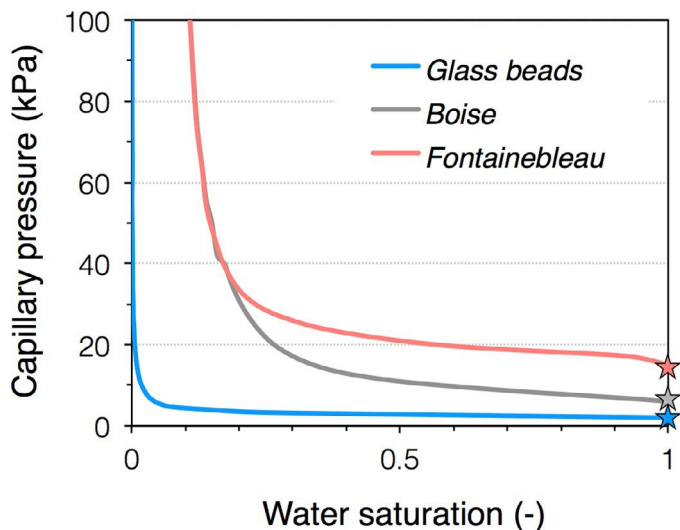
Fig. 16. Capillary pressure curves for air/water on the sintered glass beads sam-   ple (blue line), Boise sandstone (grey line) and Fontainebleau sandstone (pink line), converted from Hg/air MICP measurements. The entry pressures, represented by stars on the graphs, are about 2000 Pa for the glass beads sample, 6000 Pa for Boise sandstone and 15,000 Pa for Fontainebleau sandstone. (For interpretation of the ref- erences to color in this figure legend, the reader is referred to the web version of   this article.)

4.2. Measuring pore-scale capillary pressure

4.2.1. Capillary pressures controlled by pore structure

As expected, the mean curvature is low for trapped ganglia in the glass beads sample and significantly larger for trapped gan- glia in the Fontainebleau Sandstone in comparison to the Boise sandstone due to the pore morphology (Fig. 14). Armstrong et al. (2012a) reported curvatures of one order of magnitude lower (0.001–0.002 µm^{-1}) in a glass beads packs with much larger pores than our glass beads sample. In their study of a Ketton limestone, Andrew et al. (2014b) measured a mean curvature of 0.01 µm^{-1}, four times smaller than for the Boise sandstone sample presented here, which is also consistent since Boise presents smaller and more angular pores than the Ketton sample. To a first order, the mean curvatures values for the three samples we investigated lead to mean capillary pressures that are in good agreement with the MICP measurements for the three samples (Fig. 16). One can note that the mean capillary pressure estimated from the interfacial cur- vature between the trapped gas ganglia and the brine is in the or- der of magnitude of the entry pressure for each rock. Andrew et   al. (2014a) observed in a Ketton limestone that the curvature of the ganglia was controlled by the size of the neighboring throats. In the post-imbibition context of geological storage, it is therefore plausible that the capillary pressures of disconnected ganglia will be, to a first order, well approximated by the capillary entry pres- sure of the rock. This does not mean that the system is at equilib- rium, however.

4.2.2. Variability of capillary pressure measured on a single ganglion

The analysis of the impact of image resolution and interface identification shows that very similar curvatures are estimated for   a well-rounded gas bubble with a range of resolutions or using dif- ferent portions of the interface (Fig. 9a, Fig. 10a). The error will however be decreased when using higher resolution images and the entire interface that can be identified, leading to higher con- fidence in capillary pressure estimates (Table 3). For gas ganglia presenting more complex shapes, a different resolution can lead to a different interface identified (Fig 9b and c) and the capillary pressure of the same gas ganglia can vary from 4450 Pa to 6955 Pa

for instance for a gas ganglia from the Boise sample (Table 3a). It   can be seen on the 2D raw image displayed in the Figures that the quality of the high resolution image is significantly enhanced and the segmentation is therefore more likely to be reliable result- ing in improved curvature estimates, not to mention the fact that a same object is described by more voxels with a higher resolu- tion, thus reducing curvature calculation errors. For such gas gan- glia, the comparison between curvature values calculated using the entire identified interface or just a portion of the interface lead to noticeable variation in the curvature, hence capillary pressure es- timates exhibit similar variability (Fig. 10b, Table 3b). One possi- ble explanation to the measured differences in capillary pressures is that there are measurement errors. Estimating the curvature of the surface is the product of a series of complicated image pro- cessing steps. Uncertainty is in particular associated with image segmentation step (e.g. Wildenschild and Sheppard, 2013). A sec- ond explanation is that the interfaces are supported by a solid sur- face, and we can therefore not apply Laplace's law to link mean curvature to capillary pressure directly. A third possibility is that isolated brine/air/grain surfaces are "pinned" and represent con- tact angle hysteresis. If the capillary pressure variability across in- dividual ganglia is real, then either the pressure of the gas inside the ganglion is non-uniform, or the pressure in the liquid is non- uniform, or both are non-uniform. Non-uniform pressures do not appear likely however, especially since the brine phase is well con- nected.

In general, the standard error of the curvature values calcu- lated for all points of the interface of a ganglion is low compared with the average curvature value for the ganglion and it can be concluded that the curvature calculations yields confident capillary pressure estimates, especially for the Glass Beads dataset and the Boise and Fontainebleau imaged with the highest resolution (BS-5X dataset, and FS-10X dataset).

4.2.3. Variability of capillary pressure across a population of ganglia

This sub-section summarizes the major findings regarding the ganglia capillary pressure distributions for the two sandstones. The comparison of the exact same sub-volume of Boise sample im- aged with two different resolution (BS-2X^{+} and BS-5X^{+}) shows that more trapped gas ganglia are identified on the higher reso- lution image due mostly to the identification of a higher amount of small-size ganglia (Fig. 8, Table S2). Although for the lower res- olution image fewer interfaces are used for the curvature calcu- lation and less voxels describe these interfaces, the mean curva- ture value for the entire sub-volume does not differ much from   the one calculated on the sub- volume imaged with a higher res- olution, leading to a similar mean capillary pressure value. How- ever, the standard deviation of mean

curvature value for the dis- connected gas ganglia is two times bigger for the higher resolu- tion image, which may yield different conclusions regarding the distribution of capillary pressures and the stability of residually- trapped gas. Considering that the confidence for curvature calcula- tions is significantly increased for high-resolution images, it would be recommended to use similar voxel sizes (below 2 µm at least) for interfacial curvature analysis in sandstone rocks, as well as for any types of similar investigation such as contact angle measure- ment, in rocks presenting comparable pore structure, in particular pore bodies and throats size and shape. The analysis of the differ- ent Boise sub-volumes suggest however that there is a noticeable sampling effect probably due to the heterogeneity of the sample pore structure, leading to differences in mean capillary pressure as well as their distribution depending on the sub-volume inves- tigated. Most air ganglia have similar size and present similar cur- vature value but the amount of smaller air ganglia, which present significantly higher curvatures, varies from on sub-volume to an-

other (Fig. 14.b). Hence, the mean capillary pressure ranges from about 4600 to 7800 Pa for the same Boise sample.

For a similar number of gas ganglia investigated, Fontainebleau sandstone presents a larger number of ganglia having higher cur- vatures than the average compared with Boise sandstone (Fig. 15). Although the general mean curvature for Fontainebleau sample is higher than for Boise sample due to the pore space topology, the Fontainebleau sample does not have a higher proportion of small gas ganglia than Boise sample imaged with similar resolu- tion (BS-5X and FS-4X). The more distributed values of curvatures for Fontainebleau is likely due to the geometry of the interfaces used for the curvature calculations which present a higher degree of variability than for Boise sandstone. Even though most planar interfaces were removed for the calculation, the portions of inter- faces of interest may display significantly different curvature im- posed by the pores and throats shape, as depicted in Fig. 9c. For this type of sandstone it is important to note that the number of voxels representing the interfaces used for the curvature calcula- tion is smaller, leading to potentially higher error than for Boise sandstone, even when the calculation is done using the highest resolution sub-volume of Fontainebleau (FS-10X). In addition Fig. 9c also confirms the necessity of using a submicron voxel size for this type of sandstone in order to have more accurate results. One issue remains the very small size of sample investigated when us- ing very high image resolution and the current technical impossi- bility to perform flow experiment in a pressure vessel, necessary to investigate $scCO_2$/brine systems with reservoir conditions, using a sample size that would allow sub-micron resolution image acqui- sition. Another issue that may be raised when using a higher reso- lution is the identification of thin films of brine. Along the surface of the gas phase that is in contact with the thin films supported by the rock grains, Laplace's law is not applicable. The portion of the interface that is in contact with these films should then be removed for the purpose of capillary pressure estimation, which complicates the analysis procedure.

4.2.4. Implications for Ostwald ripening

For both sandstone samples the disconnected gas ganglia may present capillary pressures showing differences that are statisti- cally significant and Ostwald ripening would result in transferring gas from ganglia with higher capillary pressures to surrounding ganglia with lower capillary pressures.

In the case of Boise sandstone and for all the analyzed sub- volumes, the ganglia presenting higher capillary pressures consist of small gas ganglia that represent a minor fraction of the trapped gas phase. Since most other gas ganglia display almost identical capillary pressure, it can be assumed that Ostwald ripening would concern only a very small fraction of gas and would therefore not be an important mechanism for remobilizing the trapped gas in that type of sandstone.

The larger distribution in capillary pressures presented by the Fontainebleau sandstone sub-volumes would result in more gas transfer by Ostwald ripening than for Boise sandstone. However the smaller average throat dimensions and longer pore chan- nel length, characteristic of low porosity Fontainebleau sandstone (Lindquist and Venkatarangan, 2000), would significantly increase the diffusion time.

The results of this study are not intended to provide definitive conclusions one way or another regarding the potential for Ost- wald Ripening to remobilize residually trapped CO_2. Instead the goal is to develop and demonstrate experimental methods (with associated uncertainty quantification) to address the questions, do capillary pressure differences exist between gas clusters that could provide a driving force for Ostwald Ripening and can we measure them? The answer to these questions is yes: there are differences in capillary pressures between gas clusters and we can measure them. Fully addressing the question of whether or not these cap- illary pressure gradients can remobilize residually trapped CO_2 re- quires multi-physics and multi-scale modeling on a larger spatial scale than is imaged here. With regard to acquiring the data sets needed to populate and validate these models, the trade-off be- tween resolution and sample volume is evident. The larger the sample volume, the higher the probability that heterogeneities and gas cluster dimensions and topology will be fully sampled. Larger sample volumes however lead to lower spatial resolution, which results in poorer quality (and potentially erroneous) capillary pres- sure measurements. Advances in imaging technology that allow higher resolution on larger samples will be beneficial in this re- gard.

5. Conclusion

We presented a series of experiments providing multi-scale X- ray microtomography images of representative residually-trapped gas in three different sample types: a sintered glass-beads sample, a Boise sandstone sample and a Fontainebleau sandstone sample. The method to calculate interfacial curvatures was efficiently ap- plied to the three samples leading to mean capillary pressure val- ues in agreement with the literature and MICP measurements.

The analysis of the trapped gas in the two sandstones, which mostly consists of ganglia isolated to one or few pores, high- lights the impact of image resolution and interface identification on the curvature estimates. Sub-micron resolution is recommended to lead such investigation in real rocks as it increases confidence in interfacial curvature calculations due to the high number of vox- els representing the interfaces of interest. Higher resolution may however result in the identification of thin films of brine, which complicates curvature estimation.

A distribution of capillary pressures is seen for both sandstones, to a higher extent for Fontainebleau sandstone, suggesting that Ostwald ripening could occur and result in gas transfer from gan- glia having higher capillary pressures to neighbor ganglia having lower capillary pressures. However, although some small gas gan- glia may have higher capillary pressures, a high proportion of the gas phase consists of ganglia having similar capillary pressures, suggesting that Ostwald ripening could be limited for remobilizing residually-trapped gas. Likewise, we cannot determine from this experiment whether a cyclical process involving Ostwald ripen- ing could yield transport of residually-trapped CO_2 over distances greater than the pore scale.

It should however be noted that this study investigates the cap- illary pressure distribution for a single homogeneous rock, and dif- ference in pore sizes between different portion of a rock at a larger scale will result in differences in capillary pressure that could drive Ostwald ripening; this phenomenon could be particularly impor- tant for sandstones with significant laminations and sorting differ- ences.

Supplementary materials

Supplementary material associated with this article can be found, in the online version, at doi:10.1016/j.advwatres.2017.04. 006.

References

Andrew, M., Bijeljic, B., Blunt, M., 2014a. Pore-scale imaging of trapped supercritical carbon dioxide in sandstones and carbonates. Int. J. Greenhouse Gas Control 22, 1–14.

Andrew, M., Bijeljic, B., Blunt, M.J., 2014b. Pore-by-pore capillary pressure mea- surements using X-ray microtomography at reservoir conditions: Curvature, snap-off, and remobilization of residual CO2. Water Resour. Res. 50 (11), 8760–8774.

Andrew, M., Menke, H., Blunt, M.J., Bijeljic, B., 2015. The imaging of dynamic mul- tiphase fluid flow using synchrotron-based X-ray microtomography at reservoir conditions. Transp. Porous Media http://dx.doi.org/10.1007/s11242-015-0553-2.

Armstrong, R.T., Porter, M.L., Wildenschild, D., 2012a. Linking pore-scale interfacial curvature to column-scale capillary pressure. Adv. Water Resour. 46, 55–62.

Armstrong, R.T., Pentland, C.H., Berg, S., Hummel, J., Lichau, D., Bernard, L., 2012b. Estimation of curvature from micro-CT liquid-liquid displacement studies with pore scale resolution. In: *International Symposium of the Society of Core An*alysts, 27-30 August 2012. Aberdeen, Scotland, UK, pp. SCA2012–SCA2055.

Armstrong, R.T., Berg, S., 2013. Interfacial velocities and capillary pressure gradi- ents during Haines jumps. Phys. Rev. E 88, 043010. http://dx.doi.org/10.1103/ PhysRevE.88.043010.

Armstrong, R.T., Georgiadis, A., Ott, H., Klemin, D., Berg, S., 2014. Critical capillary number: Desaturation studied with fast X-ray computed microtomography. Geo- phys. Res. Lett. 41, 55–61. http://dx.doi.org/10.1002/2013GL058075.

Armstrong, R.T., McClure, J.E., Berrill, M.A., Rücker, M., Schlüter, S., Berg, S., 2016. Beyond Darcy's law: The role of phase topology and ganglion dynamics for two-phase flow. Phys. Rev. E. 94, 0433113 doi: 10.1103?PhysRevE.94.043113.

Bear, J., 1972. Dynamics of Fluids in Porous Media. Elsevier, New-York.

Blunt, M.J., Bijeljic, B., Dong, Hu, OUssama, Gharbi, Iglauer, S., Mostaghimi, P., Paluszny, A., Pentland, C., 2013. Pore-scale imaging and modeling. Adv. Water Resour. 51, 197–216.

Bourbie, T., Zinszner, B., 1985. Hydraulic and acoustic properties as a function of porosity in Fontainebleau sandstone. J. Geophys. Res 90 (n 11), 524–532.

Celia, M.A., Nordbotten, J.M., 2009. Practical modeling approaches for geological storage of carbon dioxide. Ground Water 47, 627–638.

Chaudhary, K., Cardenas, M.B., Wolfe, W.W., Maisano, J.A., Ketcham, R.A., Ben- nett, P.C., 2013. Pore-scale trapping of supercritical CO_2 and the role of grain wettability and shape. Geophys. Res. Lett. 40, 3878–3882.

Cnudde, V., and Boone, M.N., 2013. High-resolution X-ray computed tomography in geosciences: a review of the current technology and applications, Earth Science Reviews, doi:10.1016/j.earscirev.2013.04.003

Cohen-Steiner, David, Morvan, Jean-Marie, 2003. Restricted delaunay triangulations and normal cycle. In: Proceedings of the Nineteenth Annual Symposium on Computational Geometry. ACM.

DePaolo, D.J., Cole, D.R., 2013. Geochemistry of Geologic Carbon Sequestration: An Overview. Rev. Mineral. Geochem. 77, 1–14.

Desbrun, M., Meyer, M., Schroeder, P., Barr, A.H., 1999. Implicit fairing of irregular meshes using diffusion and curvature flow. In: Proceedings of the 26th annual conference on Computer graphics and interactive techniques. ACM, pp. 317–324. Dierick, M., Masschaele, B., Van Hoorebecke, L., 2004. Octopus, a fast and user-friendly tomographic reconstruction package developed in LabView®. Meas. Sci. Technol. 15, 1366–1370.

Dominguez, A., Bories, S., Prat, M., 2000. Gas cluster growth by solute diffusion in porous media. Experiments and automaton simulation on pore network. Int. J. Multiph. Flow 26, 1951–1979.

Epstein, P.S., Plesset, M.S., 1950. On the Stability of Gas Bubbles in Liquid-Gas Solu- tions. J. Chem. Phys. 18 (11), 1505–1509.

Federer, H., 1959. Curvature measures. Trans. Am. Math. Soc. 93 (3), 418–491.

Garing, C., Voltolini, M., Ajo-Franklin, J.B., Benson, S.M., 2017. Residual air in air/brine systems, Dataset uploaded to Digital Rocks Portal. University of Texas at Austin, http://dx.doi.org/10.17612/P7ZW24.

Georgiadis, A., Berg, S., Makurat, A., Maitland, G., Ott, H., 2013. Pore-scale micro- computed-tomography imaging: Nonwetting-phase cluster-size distribution dur- ing drainage and imbibition. Phys. Rev. E 88. http://dx.doi.org/10.1103/PhysRevE. 88.033002.

Goldobin, D.S., Brilliantov, N.V., 2011. Diffusive counter dispersion of mass in bubbly media. Phys. Rev. E 84 (5), 056328.

Goodman, A., Hakala, A., Bromhal, G., Deel, D., Rodosta, T., Frailey, S., Small, M., Allen, D., Romanov, V., Fazio, J., Huerta, N., McIntyre, D., Kutchko, B., Guthrie, G., 2011. US DOE methodology for the development of geologic storage potential for carbon dioxide at the national and regional scale. Int. J. Greenhouse Gas Control 5, 952–965.

Greenwood, A., 1956. The growth of dispersed precipitates in solutions. Acta Mel- laturgica 4, 243–248.

Hamon, G., Suzanne, K., Billiotte, J, Trocme, V., 2001. Field-Wide Variations of Trapped Gas saturation in Heterogeneous Sandstone Reservoirs. SPE, p. 71524.

Herring, A.L., Andersson, L, Wildenschild, D., 2016. Enhancing residual trapping of supercritical CO_2 via cyclic injections. Geophys. Res. Lett. 43 (n 18), 9677–9685. http://dx.doi.org/10.1002/2016GL070304.

Hesse, M.A., Orr Jr, F.M., Tchelepi, H.A., 2008. Gravity currents with residual trap- ping. J. Fluid Mech. 611, 35–60.

Iglauer, S., Paluszny, A., Pentland, C.H., Blunt, M., 2011. Residual CO2 imaged with X-ray micro-tomography. Geophys. Res. Lett. 38. http://dx.doi.org/10.1029/ 2011GL049680.

Juanes, R., Spiteri, E.J., Orr Jr, F.M., Blunt, M., 2006. Impact of relative permeability hysteresis on geological CO2 storage. Water Resour. Res. 42, W12418. http://dx. doi.org/10.1029/2005WR004806.

Kak, A.C., and Slaney, M. 1987. Principles of computerized tomographic imaging.

Kim, Y., Wan, J., Kneafsey, T.J., Tokunaga, T.K., 2012. Dewetting of silica surfaces upon reactions with supercritical CO_2 and brine: pore-scale studies in micromodels. Environ. Sci. Technol. 46 (7), 4228–4235.

Kroon, D., 2011. Patch Curvature. http://www.mathworks.com/matlabcentral/ fileexchange/32573-patch-curvature.

Kumar, A., Ozah, R., Noh, M., Pope, G.A., Bryant, S., Sepehrnoori, K., Lake, L.W., 2005. Reservoir simulation of CO_2 storage in deep saline aquifers. SPE Journal 10 (3), 336–348 n.

Kumar, M., Senden, T.J., Sheppard, A., Middleton, J.P., Knackstedt, M.A., 2010. Vizual- izing and quantifying the residual phase distribution in core material. Petro- physics 51 (5), 323–332.

Li, X., Yortsos, Y.C., 1991. Visualization and Numerical Studies of Bubble Growth dur- ing Pressure Depletion. SPE Annu. Tech. Conf. Exhib. 6-9 (October).

Li, X., Yortsos, Y.C., 1995. Theory of multiple bubble growth in porous media by solute diffusion. Chem. Eng. Sci. 50 (8), 1247–1271.

Lifshitz, I.M., Slyozov, V.V., 1961. The kinetics of precipitation from supersaturated solid solutions. J. Phys. Chem. Solids 19 (1-2), 35–50.

Lindquist, W.B., Venkatarangan, A., 2000. Pore and throat size distributions mea- sured from synchrotron X-ray tomographic images of Fontainebleau sandstones. J. Geophys. Res. 105 (B9) 21,509-21,527.

McClure, J.E., Berrill, M.A., Gray, W.G., Miller, C.T., 2016a. Tracking interface and com- mon curvature dynamics for two-fluid flow in porous media. J. Fluid Mech, col. 796, 211–232. http://dx.doi.org/10.1017/jfm.2016.212.

McClure, J.E., Berrill, M.A., Gray, W.G., Miller, C.T., 2016b. Influence of phase connec- tivity on the relationship among capillary pressure, fluid saturation and inter- facial area in two-fluid-phase porous medium systems. Phys. Rev. E 94, 033102. http://dx.doi.org/10.1103/PhysRevE.94.033102.

Möller, J., Jacob, K., Schmelzer, J., 1998. Ostwald ripening in porous viscoelastic ma- terials. J. Phys. Chem. Solids 59 (6-7), 1097–1103.

Paganin, D., Mayo, S.G., Gureyev, T.E., Miller, P.R., Wilkins, S.W., 2002. Simoultaneous phase and amplitude extraction from a single defocused image of a homoge- neous object. J. Microscopy 206 (1), 33–40.

Peyre, G., 2007. Graph theory toolbox. http://www.mathworks.com/matlabcentral/ fileexchange/5355-toolboxgraph?s_tid=srchtitle.

Prasad, M., 2001. Mapping impedance microstructures in rocks with acoustic mi- croscopy. Leading Edge 20 (2), 172–179.

Prodanovic, M., Lindquist, W.B., Seright, R.S., 2007. 3D image-based characterization of fluid displacement in a Berea core,. Adv. Water Resour. 30, 214–226.

Prodanovic, M., Esteva, M., Hanlon, M., Nanda, G., Agarwal, P., 2015. Digital Rocks Portla: a repository for porous media images, http://dx.doi.org/10.17612/P7CC7K. Rücker, M., Berg, S., Armstrong, R.T., Georgiadis, A., Ott, H., Schwing, A., Neiteler, R., Brussee, N., Makurat, A., Leu, L., Wolf, M., Khan, F., Enzmann, F., Kersten, M., 2015. From connected pathway flow to ganglion dynamics. Geophys. Res. Lett. 42, 3888–3894. http://dx.doi.org/10.1002/2015GL064007.

Schlüter, S., Sheppard, A.P., Brown, K., Wildenschild, D., 2014. Image processing of multiphase images obtained via X-ray microtomography: A review. Water Re- sour. Res. 50 (4), 3615–3639 n.

Schlüter, S., Berg, S., Rücker, M., Arsmtrong, R.T., Vogel, H.J., Hilfer, R., Wilden- schild, D., 2016. Pore-scale displacement mechanisms as a source of hystere- sis for two-phase flow in porous media. Water Resour. Res. 52, 2194–2205. http://dx.doi.org/10.1002/2015WR018254.

Schmelzer, J., Schweitzer, F., 1987. Ostwald Ripening of Bubbles in Liquid-Gas Solu- tions. J. Non-Equilibrium Thermodyn. 12 (3), 255–270 n.

Schmelzer, J., Möller, J., Slezov, J.J., 1995. Ostwald ripening in porous materials: The case of arbitrary pore size distributions. J. Phys. Chem. Solids 56 (8), 1013–1022 n.

Sok, R.M., Knackstedt, M.A., Sheppart, A.P., Pinczewski, W.V., Lindquist, W.B., Venkatarangan, A., Paterson, L., 2002. Direct and stochastic generation of net- work models from tomographic images; effect of topology on residual satura- tions. Transp. Porous Media 46, 345–372.

Sorkine, O., 2006. Differential representations for mesh processing. Comput. Graph- ics Forum 25 (4), 789–807 n.

Tanino, Y, Blunt, M.J., 2012. Capillary trapping in sandstones and carbonates: De- pendence on pore structure. Water Resour. Res. 48 (8), 1–13 n.

Tomasi, C., Maduchi, R., 1998. Bilateral filtering for gray and color images. In: 6th International Conference on Computer Vision, pp. 839–846.

Vargaftik, N.B., Volkov, B.N., Voljak, L.D., 1983. International tables of the surface tension of water. J. Phys. Chem. Ref. Data 12 (3), 817–820 n.

Voorhees, P.W., 1985. The theory of Ostwald Ripening. J. Stat. Phys. 38 (1-2), 231–252.

Wan, J., Kim, Y., Tokunaga, T.K., 2014. Contact angle measurement ambiguity in su- percritical CO_2–water–mineral systems: Mica as an example. Int. J. Greenhouse Gas Control 31, 128–137.

Wang, S., Tokunaga, T.K., Wan, J., Dong, W., Kim, Y., 2016. Capillary pressure-satura- tion relations in quartz and carbonate sands: Limitations for correlating capil- lary and wettability influences on air, oil, and supercritical CO2 trapping. Water Resour. Res. 52 (2), 6671–6690 n.

Weitkamp, T., Haas, D., Wegrzynek, D., Rack, A., 2011. ANKAphase: software for sin- gle-distance phase retrieval from inline X-ray phase contrast radiographs. J. Syn- chrotron Radiation 18 (4), 617–629 n.

Wildenschild, D., Sheppard, A.P., 2013. X-ray imaging and analysis techniques for quantifying pore-scale structure and processes in subsurface porous medium systems. Adv. Water Resour. 51, 217–246.

Zimmerman, R.W., 1984. The Effect of Pore Structure On the Pore and Bulk Compressibilities of Consolidated sandstones. University of California, Berkeley, p. 116.